



**HAL**  
open science

## Locally Generated ULF Waves in the Martian Magnetosphere: MAVEN Observations

Y. Harada, S. Ruhunusiri, J. S. Halekas, J. Espley, G. A. Dibraccio, J. P. Mcfadden, D. L. Mitchell, C. Mazelle, G. Collinson, D. A. Brain, et al.

► **To cite this version:**

Y. Harada, S. Ruhunusiri, J. S. Halekas, J. Espley, G. A. Dibraccio, et al.. Locally Generated ULF Waves in the Martian Magnetosphere: MAVEN Observations. *Journal of Geophysical Research Space Physics*, 2019, 124, pp.8707-8726. 10.1029/2019JA027312 . insu-03674387

**HAL Id: insu-03674387**

**<https://insu.hal.science/insu-03674387>**

Submitted on 21 May 2022

**HAL** is a multi-disciplinary open access archive for the deposit and dissemination of scientific research documents, whether they are published or not. The documents may come from teaching and research institutions in France or abroad, or from public or private research centers.

L'archive ouverte pluridisciplinaire **HAL**, est destinée au dépôt et à la diffusion de documents scientifiques de niveau recherche, publiés ou non, émanant des établissements d'enseignement et de recherche français ou étrangers, des laboratoires publics ou privés.

Copyright

# JGR Space Physics

## RESEARCH ARTICLE

10.1029/2019JA027312

### Key Points:

- MAVEN observes narrow band ULF waves near the local proton cyclotron frequency below the Martian bow shock
- Compressional narrow band emissions are newly identified in the dayside upper ionosphere and in the nightside magnetotail
- The wave-particle interaction facilitates energy transfer from hot protons of magnetosheath origin to cold ionospheric protons

### Correspondence to:

Y. Harada,  
 haraday@kugi.kyoto-u.ac.jp

### Citation:

Harada, Y., Ruhunusiri, S., Halekas, J. S., Espley, J., DiBraccio, G. A., McFadden, J. P., et al. (2019). Locally generated ULF waves in the Martian magnetosphere: MAVEN observations. *Journal of Geophysical Research: Space Physics*, 124, 8707–8726. <https://doi.org/10.1029/2019JA027312>

Received 17 AUG 2019

Accepted 13 OCT 2019

Accepted article online 12 NOV 2019

Published online 14 NOV 2019

Corrected 25 MAR 2020

This article was corrected on 25 MAR 2020. See the end of the full text for details.

## Locally Generated ULF Waves in the Martian Magnetosphere: MAVEN Observations

Y. Harada<sup>1</sup>, S. Ruhunusiri<sup>2</sup>, J. S. Halekas<sup>2</sup>, J. Espley<sup>3</sup>, G. A. DiBraccio<sup>3</sup>, J. P. McFadden<sup>4</sup>, D. L. Mitchell<sup>4</sup>, C. Mazelle<sup>5</sup>, G. Collinson<sup>3,6</sup>, D. A. Brain<sup>7</sup>, T. Hara<sup>4</sup>, M. Nosé<sup>8</sup>, S. Oimatsu<sup>1</sup>, K. Yamamoto<sup>1</sup>, and B. M. Jakosky<sup>7</sup>

<sup>1</sup>Department of Geophysics, Kyoto University, Kyoto, Japan, <sup>2</sup>Department of Physics and Astronomy, University of Iowa, Iowa City, IA, USA, <sup>3</sup>NASA Goddard Space Flight Center, Greenbelt, MD, USA, <sup>4</sup>Space Sciences Laboratory, University of California, Berkeley, CA, USA, <sup>5</sup>IRAP, University of Toulouse, CNRS, UPS, CNES, Toulouse, France, <sup>6</sup>Institute for Astrophysics and Computational Sciences, The Catholic University of America, Washington, DC, USA, <sup>7</sup>Laboratory for Atmospheric and Space Physics, University of Colorado, Boulder, CO, USA, <sup>8</sup>Institute for Space-Earth Environmental Research, Nagoya University, Nagoya, Japan

**Abstract** We investigate Martian ultralow frequency (ULF) electromagnetic waves generated by local plasma instabilities below the Martian bow shock. Recent Mars Atmosphere and Volatile Evolution (MAVEN) observations have shown that ULF waves generated upstream of the Martian bow shock can propagate down to the upper ionosphere, possibly facilitating heavy ion escape from Mars by heating the ionospheric plasma. In contrast to the upstream waves oscillating near the *upstream* proton cyclotron frequency, we identify narrow band ULF magnetic field fluctuations with frequencies near the *local* proton cyclotron frequency ( $f_{cp(local)}$ ) from MAVEN data. In addition to expected proton cyclotron waves locally generated in the magnetosheath, we newly identify compressional narrow band emissions near  $f_{cp(local)}$  (and its harmonics for some cases) in the dayside upper ionosphere and in the nightside magnetotail. The dayside waves are preferentially observed for high solar extreme ultraviolet (EUV) conditions and are often associated with ring/shell-like, hot protons of magnetosheath origin in the presence of cold, dense ionospheric protons. The nightside waves exhibit distinct preference for high-solar-EUV, strong-solar-wind conditions, under which both warm and cold protons are enhanced. The observed properties of these compressional waves are generally consistent with a proton Bernstein mode instability driven by a positive perpendicular slope in proton velocity distribution functions. The excited waves can cause perpendicular heating of thermal protons, thereby transferring energy from precipitating hot protons to cold ionospheric protons.

### 1. Introduction

The upper atmosphere of Mars is directly exposed to the solar wind as a consequence of the lack of a strong, intrinsic magnetic field. Energy deposition from the solar wind and solar radiation facilitates atmospheric loss to space in forms of neutral and ion escape, which could have played a crucial role in the evolution of the Martian atmosphere (e.g., Jakosky et al., 2018). Energization of ions in the Martian upper ionosphere and its dependence on upstream drivers are yet to be fully characterized (Dubinin et al., 2012, 2017; Lundin, 2011; Ramstad et al., 2017), and this represents one of the major difficulties in elucidating the atmospheric evolution of Mars.

As the complexity and dynamic nature of the Martian magnetosphere have been revealed (DiBraccio et al., 2018; Halekas et al., 2015; Ruhunusiri et al., 2016), the importance of identifying and understanding each channel of energy flows carried by particles and fields in the near Mars space has become increasingly recognized. For instance, recent observations showed that narrow band ultralow frequency (ULF) waves generated upstream of the bow shock propagate all the way through the magnetosheath down to the dayside upper ionosphere, wherein wave-particle interaction causes significant heating of ionospheric heavy ions (Collinson et al., 2018; Fowler et al., 2017, 2018). These waves of upstream origin typically oscillate near the upstream proton cyclotron frequency ( $f_{cp(upstream)}$ ) with left-handed polarizations in the spacecraft frame (which approximately corresponds to the Mars rest frame), and they are interpreted as intrinsically right-handed waves propagating upstream in the solar wind frame, presumably resonating with newborn

pickup protons or reflected solar wind protons (Romanelli et al., 2016; Ruhunusiri et al., 2016). Note that  $f_{\text{cp(upstream)}}$  could be around the local cyclotron frequencies of oxygen ions in the dayside ionosphere as a result of the piled-up and compressed magnetic field therein.

This paper reports on Mars Atmosphere and Volatile EvolutionN (MAVEN) observations of different classes of electromagnetic ULF waves at Mars. In contrast to the relatively well-studied upstream waves (Brain et al., 2002; Mazelle et al., 2004; Romanelli et al., 2013, 2016; Ruhunusiri et al., 2016; Wei & Russell, 2006), we focus on narrow band magnetic field fluctuations near and just below the local proton cyclotron frequency ( $f_{\text{cp(local)}}$ ) observed downstream of the bow shock. Several wave populations are identified in different plasma regimes around Mars, i.e., the dayside upper ionosphere, nightside magnetotail, and magnetosheath. As implied by their association with  $f_{\text{cp(local)}}$ , many of the observed properties can be understood in terms of wave generation by local proton instabilities. Of the identified wave populations, waves in the dayside upper ionosphere may be of a particular interest, because they can deposit energy to cold, dense ionospheric protons.

## 2. Data Analysis

We utilize magnetic field and plasma data obtained by the MAVEN mission (Jakosky et al., 2015) from 1 December 2014 to the end of 2018, spanning over two Martian years. For each MAVEN orbit, we analyze data obtained from 48 min before to 48 min after the periapsis (typically below  $\sim 3,000$  km altitudes). We mainly use magnetic field data obtained by the magnetometer (MAG; Connerney et al., 2015) and proton and heavy ion velocity distributions obtained by the SupraThermal and Thermal Ion Composition (STATIC) instrument (“d0” and “d1” data products; see McFadden et al., 2015). We also present ion data from the Solar Wind Ion Analyzer (SWIA; Halekas et al., 2015) and electron data from the Solar Wind Electron Analyzer (SWEA; Mitchell et al., 2016) to provide context for wave observations.

We apply the fast Fourier transform to 32 vector samples per second magnetic field data sliding a 64 s (2,048 samples) Hanning window by 4 s. For each window, the background magnetic field direction is determined from the average magnetic field, and we compute the compressional (parallel to the background field) and transverse (perpendicular to the background field) wave powers. Figure 1 shows a sample time series of MAVEN data. The frequency-time spectrograms of the total (compressional plus transverse) wave power and compressional to total power ratio are shown in Figures 1g and 1h, respectively. In addition to the wave powers, we estimate wave vector direction and ellipticity from the complex spectral matrix averaged over seven frequencies with Hanning weighting by utilizing the singular value decomposition technique (Santolík et al., 2003; Taubenschuss & Santolík, 2019). The estimated wave normal angle with respect to the background magnetic field and ellipticity (+1 means right-handed circular polarization) are shown in Figures 1i and 1j, respectively.

We perform an automated search for narrow band magnetic field fluctuations near  $f_{\text{cp(local)}}$  from the aforementioned data set. Our wave detection algorithm works as follows: For each measured spectrum, the total power spectrum is trimmed to a frequency range of  $0.25f_{\text{cp(local)}} < f < 1.5f_{\text{cp(local)}}$  and at  $f \geq 0.0625$  Hz. This frequency range is chosen such that we can efficiently identify narrow band waves near  $f_{\text{cp(local)}}$  and yet ensure sufficient margins to avoid edge effects. From the trimmed spectrum, we identify a tentative wave event with a spectral peak if (i) the peak power exceeds  $0.1 \text{ nT}^2/\text{Hz}$  and (ii) the peak power is at least an order of magnitude greater than the minimum power on either side of the peak. If multiple peaks satisfy Conditions (i) and (ii), we select one with the strongest power as a tentative wave event. We then select wave events that are persistent for at least 16 consecutive spectra with frequency jumps from one peak to the next smaller than a factor of 1.5. We tuned this algorithm conservatively to reduce contamination from turbulent fluctuations with transient peaks by only selecting persistent, long-duration wave events. We note that artificial tones caused by reaction wheel assemblies are typically much weaker than the power threshold of our choice ( $0.1 \text{ nT}^2/\text{Hz}$ ). The magenta and cyan dots in Figures 1g–1j represent narrow band wave events identified by our algorithm.

To organize the wave observations by upstream solar wind conditions, we derive upstream solar wind parameters for each MAVEN orbit from SWIA and MAG measurements by utilizing an algorithm that automatically identifies time intervals during which the spacecraft is located in the solar wind plasma (Halekas et al., 2016). For the solar extreme ultraviolet (EUV) input, we use 121–122 nm photon flux measured by the Extreme Ultraviolet Monitor (EUVM; Eparvier et al., 2015).

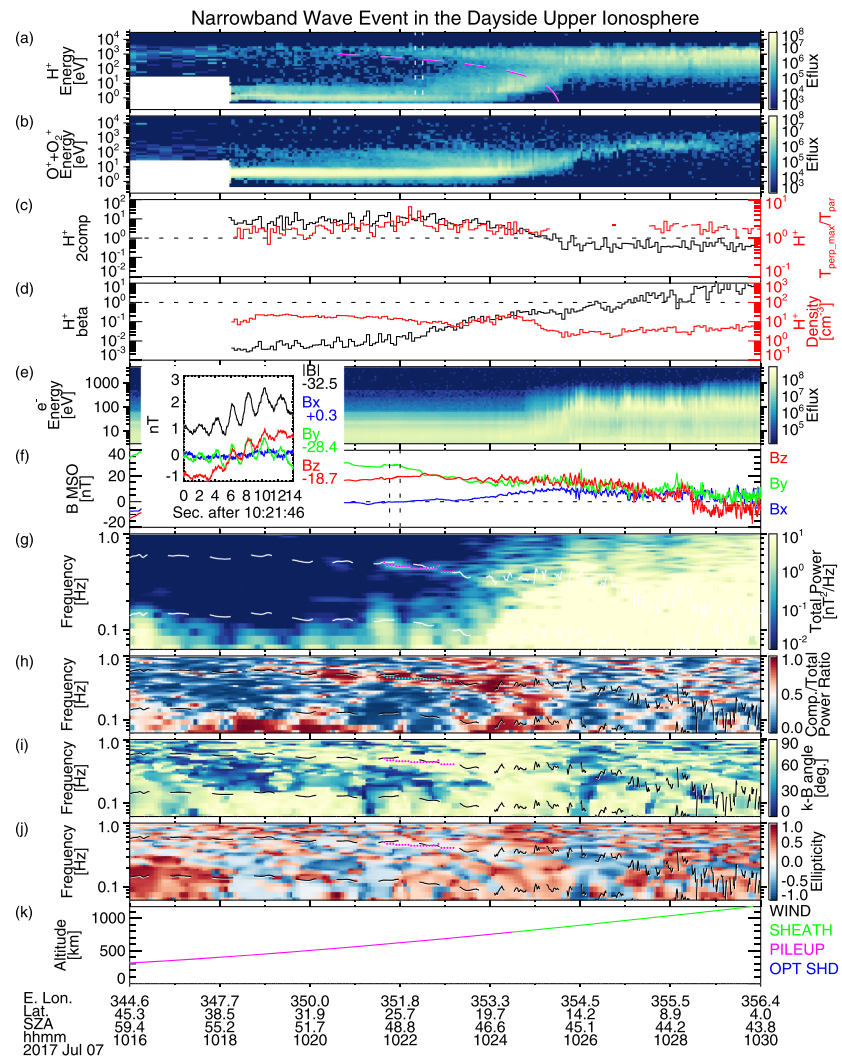


**Figure 1.** MAVEN observations during 10:16–10:30 UT on 7 July 2017 of (a)  $H^+$  energy spectra in units of differential energy flux (Eflux) of  $eV/cm^2/s/sr/eV$  obtained by STATIC, (b)  $O^+$  and  $O_2^+$  energy spectra, (c)  $H^+$  two-component parameter and temperature anisotropy (see text for detail), (d)  $H^+$   $\beta$  and density, (e) electron energy spectra, (f) magnetic field in Mars Solar Orbital (MSO) coordinates, (g) magnetic field total wave power, (h) compressional to total power ratio, (i) wave normal angle with respect to the background magnetic field, (j) ellipticity (+1 = right-handed circular polarization), and (k) spacecraft altitude color coded by nominal plasma regimes (Trotignon et al., 2006). The east longitude, latitude, and solar zenith angle of the spacecraft location are shown in the text label. The magenta dashed lines in Figure 1a indicate the estimated lowest energy at which gyrating magnetosheath protons can reach the spacecraft below the magnetic pileup boundary. The upper and lower dashed lines in Figures 1g–1j denote the local  $H^+$  and  $He^+$  cyclotron frequencies, respectively. The magenta and cyan dots in Figures 1g and 1h indicate the narrow band waves identified by our selection algorithm. The insert shows the waveform during the time intervals indicated by the vertical dotted lines in Figure 1f.

### 3. Case Studies

In this section, we present representative cases of the identified narrow band waves around  $f_{cp(local)}$  along with plasma measurements in the dayside upper ionosphere, nightside magnetotail, and magnetosheath.

#### 3.1. Waves in the Dayside Upper Ionosphere

Figure 1 presents a  $f \sim f_{cp(local)}$  wave event observed in the dayside upper ionosphere. Figure 1g shows the presence of a narrow band peak in the wave power with frequencies close to  $f_{cp(local)}$  (upper dashed line). The insert of Figure 1 demonstrates a quasi-sinusoidal waveform as inferred from the narrow band spectral peak. This wave is characterized by the dominance of the compressional wave power (Figure 1h). Consequently, the wave is estimated to propagate at angles almost perpendicular to the background magnetic field

(Figure 1i) with nearly linear polarization (Figure 1j). We note that the Doppler shift is expected to be small for this event because of low flow velocities of cold ionospheric plasma, characteristics of which will be described in the following. The close association of the wave frequency with  $f_{cp(\text{local})}$  (Figure 1g) suggests the local wave generation by a proton instability.

Plasma measurements during this wave event are shown in Figures 1a–1e. During this time interval, MAVEN traveled from the dayside upper ionosphere (also known as the magnetic pileup region, MPR) out to the magnetosheath (see the nominal plasma regimes at the spacecraft location from Trotignon et al., 2006, shown in colors in Figure 1k). The MPR is characterized by draped and piled-up interplanetary magnetic fields (Nagy et al., 2004), displaying elevated magnetic field magnitude with relatively smooth variations (Figure 1f). The MPR is generally populated by plasma of ionospheric origin, and it is separated from the shocked solar wind plasma in the magnetosheath by the magnetic pileup boundary (MPB; see also Espley, 2018). For this event, we can identify the MPB crossing between 10:25–10:26 UT. As expected, we see low proton  $\beta$  in the MPR, where the magnetic pressure dominates, and high proton  $\beta$  of  $>\sim 1$  in the magnetosheath with high proton thermal pressures (Figure 1d). The transition from the upper ionosphere to the magnetosheath is seen as the changes in dominant particle populations from the cold protons and heavy ions of ionospheric origin to hot protons of solar wind origin (Figures 1a and 1b) and from ionospheric photoelectrons to hot electrons of solar wind origin (Figure 1e). Along the way, MAVEN detected distinct two peaks in the proton energy spectra below the MPB, one at high energies of  $\sim 1$  keV and one at low energies at  $\sim 1$  eV (Figure 1a). We point out that the lower energy cutoff of the high-energy component descends as the spacecraft approaches the MPB.

To quantify the coexistence and distinct separation of the hot and cold proton components in preparation for statistical studies, we define a proton two-component parameter based on the ratios of proton fluxes in three different energy bands:  $1/(F_{25-50\text{eV}}/F_{<25\text{eV}} + F_{25-50\text{eV}}/F_{>50\text{eV}})$ , where  $F$  is obtained by integrating the differential number flux over the corresponding energy range and adding a constant offset of  $10^4 \text{ cm}^{-2} \text{ s}^{-1} \text{ st}^{-1}$  to it. This artificial offset is added to prevent noisy fluctuations of the flux ratios for extremely small fluxes with low counting statistics. We design this parameter such that it becomes  $\gg 1$  only when significant ( $>10^4 \text{ cm}^{-2} \text{ s}^{-1} \text{ st}^{-1}$ ) fluxes are recorded at both low ( $<25$  eV) and high ( $>50$  eV) energies with a flux minimum at intermediate energies (25–50 eV). When only one component is present, the two-component parameter becomes  $\leq 1$ . To ensure energy coverage, we exclude STATIC data from two-component parameter computation if the lowest measured energy is above 2 eV or the highest measured energy is below 1 keV. The black line in Figure 1c shows the proton two-component parameter computed from the measured proton energy spectra (Figure 1a), demonstrating that the two-component parameter of  $\gg 1$  successfully indicates the coexistence of well-separated hot and cold proton components. Additionally, we estimate proton temperature anisotropy,  $T_{\perp}/T_{\parallel}$ , from STATIC data (Figure 1c) by accounting for the limited field of view (i.e., taking the maximum value of the diagonalized perpendicular pressure tensor for  $P_{\perp}$  and selecting data with the magnetic field direction within the STATIC field of view in the same manner as Halekas et al. (2017)).

The energies of the hot proton component ( $\sim 100$ – $1,000$  eV) observed below the MPB imply that these protons originate from the magnetosheath (e.g., Diéval et al., 2013; Lundin et al., 2004). We note that the protons of magnetosheath origin could include pickup protons of exospheric origin in addition to protons of solar wind origin and that distinguishing them is not necessarily straightforward (Diéval et al., 2012). Some of the hot magnetosheath protons can cross the MPB owing to their nonzero gyroradii. Higher-energy protons with larger gyroradii can penetrate deeper into the MPR. At a given spacecraft location below the MPB, we can estimate the critical (lowest) energy of the magnetosheath protons,  $E_c$ , by equating the proton gyrodiameter and the normal distance from the MPB,  $2\sqrt{2mE_c}/(eB) = d_n$ , where  $m$  is the proton mass,  $e$  is the elementary charge,  $B$  is the magnetic field magnitude, and  $d_n$  is the distance from the MPB in the boundary normal direction. Assuming a stationary, spherical boundary (note that the nominal MPB shape is not much different from a sphere on the dayside; Trotignon et al., 2006), we approximate  $d_n$  by the altitude difference from the MPB crossing (taken at 10:25:37 UT). The computed  $E_c$  is shown by the magenta dashed line in Figure 1a. The predicted  $E_c$  agrees well with the measured lowest energy of the hot proton component, suggesting that the hot proton component consists of magnetosheath protons penetrating the MPB with the help of their large gyroradii.

Figure 2 shows a slice of the proton velocity distribution function (VDF),  $f_p(\mathbf{v})$ , obtained by STATIC during 10:22:19–10:22:31 UT (denoted by the vertical dotted lines in Figure 1a) on the  $v_{\parallel}$ - $v_{\perp, \text{LXMSO}}$  plane, which

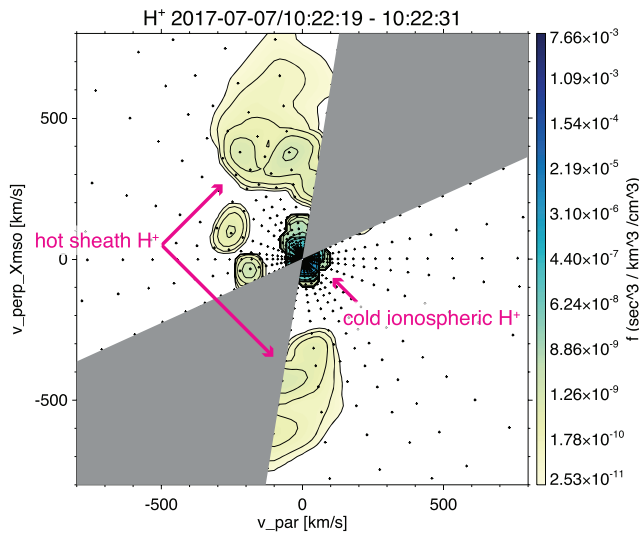


**Figure 2.** Slice of the proton velocity distribution function on the  $v_{\perp}$ - $v_{\perp X_{MSO}}$  plane obtained during 10:22:19-10:22:31 UT on 7 July 2017 (denoted by the vertical dotted lines in Figure 1a). The black plus signs indicate the data points used to produce the contour plot. The gray areas display the invisible directions outside of the unblocked STATIC field of view.

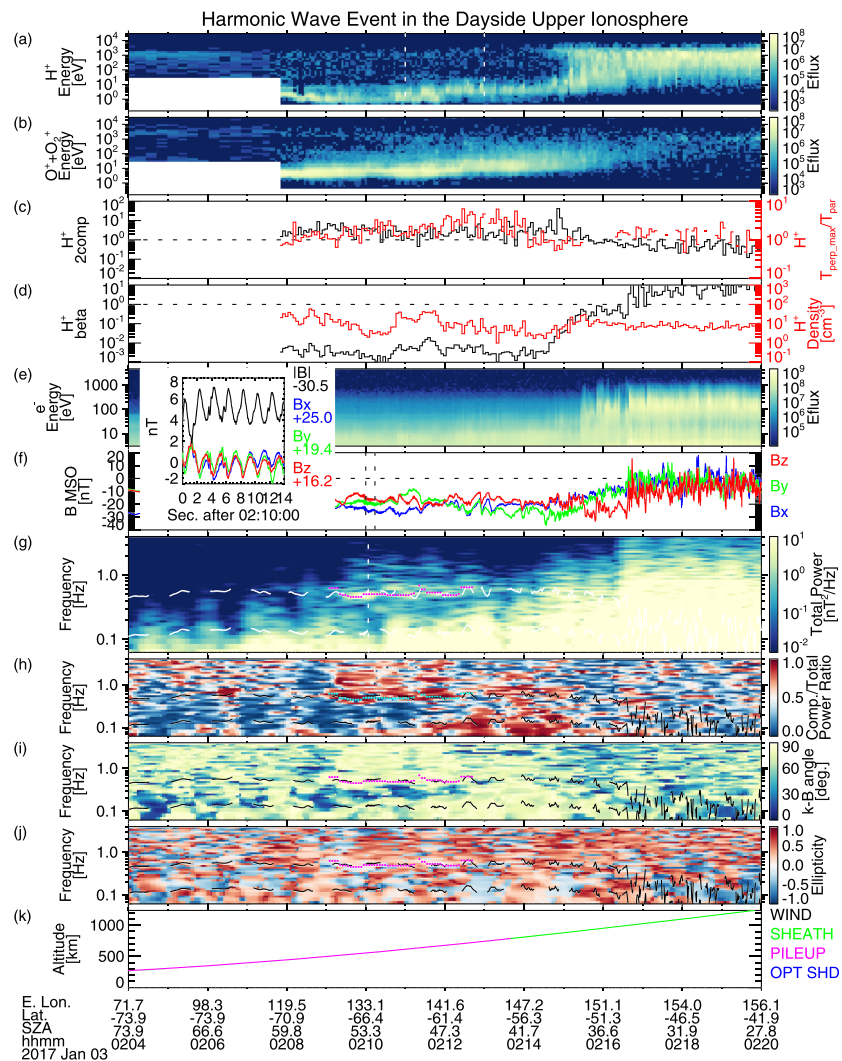
includes both the local magnetic field and  $X_{MSO}$  directions ( $+v_{\perp X_{MSO}}$  corresponds to the sunward velocity component perpendicular to the magnetic field). We observe the hot protons at  $v_{\parallel} \sim 0$  and  $|v_{\perp X_{MSO}}| > 200$  km/s, which are clearly separated from the cold proton component. The presence of both sunward and antisunward perpendicular protons is consistent with the gyrating protons of magnetosheath origin. These perpendicular hot protons lead to high proton temperature anisotropy of  $\sim 2$ – $5$  during this time interval (Figure 1c). We point out that the cold ionospheric protons also show an anisotropic distribution elongated in the perpendicular direction. This proton VDF measured concurrently with the compressional wave closely resembles proton ring distributions that are often associated with narrow band, compressional ULF waves with frequencies around  $f_{cp(local)}$  harmonics observed near the magnetic equator in the terrestrial magnetosphere (also known as “equatorial noise” and “magnetosonic waves”; e.g., Gurnett, 1976; Meredith et al., 2008; Perraut et al., 1982; Posch et al., 2015; Russell et al., 1970). This type of proton VDF has a positive perpendicular slope,  $\partial f_p(v_{\perp})/\partial v_{\perp} > 0$ , at  $v_{\parallel} \sim 0$ . If the positive perpendicular slope is sufficiently steep, the proton VDF becomes unstable to a proton Bernstein mode instability (e.g., Gary et al., 2011). We will discuss sources of the narrow band waves in section 5.

Figure 3 presents another wave event observed in the dayside upper ionosphere. MAVEN detected narrow-band waves with frequencies near  $f_{cp(local)}$  (Figure 3g) in the predominantly compressional power (Figure 3h) at almost perpendicular propagation angles (Figure 3i) with small, mixed ellipticity (Figure 3j). We observe harmonic structures above  $f_{cp(local)}$  for this event. Figure 4a shows a snapshot of compressional and transverse wave spectra at the center acquisition time indicated by the vertical dotted line in Figure 3g. We can identify at least three harmonic peaks at  $\sim f_{cp(local)}$ ,  $2f_{cp(local)}$ , and  $3f_{cp(local)}$ . Consistent with the multiple harmonics, the waveform is distorted from a sinusoidal form as shown in the insert of Figure 3. The spectral peaks near the harmonics of  $f_{cp(local)}$  and propagation angles nearly perpendicular to the background magnetic field are consistent with the proton Bernstein mode instability (Gary et al., 2011; Perraut et al., 1982). We note that the harmonic peaks above  $f_{cp(local)}$  tend to have right-handed polarizations (Figure 3j), which is consistent with terrestrial observations and cold plasma theory (Perraut et al., 1982). Although clear harmonic structures are not typically seen in the wave events identified at Mars, we found at least several other events with similar peaks above  $f_{cp(local)}$ .

This wave event is also accompanied by two-component protons (Figures 3a and 3c), but the hot component has much lower fluxes with more diffuse energy spectra compared to the distinct high-energy peak seen in Figure 1a. Figure 4b shows a slice of the proton VDF obtained during the time interval denoted by the vertical dotted lines in Figure 3a. The proton VDF indicates the presence of parallel and perpendicular hot protons, forming a partial shell in the antisunward direction. These parallel protons detected deep in the MPR cannot be explained by the simple scenario of perpendicular entry of gyrating magnetosheath protons. The magnetic field observed in the MPR for this event (Figure 3f) is not as smooth as that in Figure 1f, implying that spatial variability of the piled-up magnetic field with scale lengths comparable to or smaller than the proton gyroradii may give rise to a more complex entry path. Nevertheless, we point out that the measured proton VDF displays a hint of a positive perpendicular slope at  $(v_{\parallel}, v_{\perp X_{MSO}}) \sim (0, -300)$  km/s.

### 3.2. Waves in the Nightside Magnetotail

Next we present a narrow band wave event observed in the nightside magnetotail (Figure 5). As indicated by the magenta dots in Figures 5h–5k, we observe narrow band waves just below  $f_{cp(local)}$  with predominantly compressional power, nearly perpendicular propagation angles, and small ellipticity. Harmonic structures are evident for this event as shown by Figure 6a, consistent with the highly distorted waveform as seen in the insert of Figure 5. This wave event was observed in the magnetotail lobe with sunward magnetic fields (Figure 5g) with low proton  $\beta$  (Figure 5d). Coinciding with the identified waves, MAVEN detected warm



**Figure 3.** MAVEN observations during 02:04–02:20 UT on 3 January 2017 in the same format as Figure 1.

protons at  $\sim 100$  eV (Figure 5a) with proton two-component parameter of  $\leq 1$  and temperature anisotropy of  $> 1$  (Figure 5c). The electron pitch angle distributions display one-sided loss cones on the antiparallel side (Figure 5f), indicating an open magnetic field topology with the parallel end of the field line connected to the collisional atmosphere.

Figure 6b shows a slice of the proton VDF at 15:06:58–15:08:02 UT (indicated by the vertical dotted lines in Figure 5a), when the narrow band wave was detected. As illustrated by the magenta oval, we observe a bite out of antiparallel warm protons. The coincident absence of antiparallel warm protons and electrons suggests that the warm protons are of magnetosheath origin and some of the incident protons are absorbed in the collisional atmosphere, giving rise to an antiparallel loss cone in the proton VDF. We note that aside from the antiparallel loss cone, the suprathermal protons show an elongated distribution in the perpendicular direction. Meanwhile, the presence of cold heavy ions (Figure 5b) implies that cold ionospheric protons may also be present at low energies despite the lack of distinct two peaks in the proton energy spectra (Figure 5a). A positive perpendicular slope near the edge of a large proton loss cone can be unstable to a proton Bernstein mode instability, which can partly account for the compressive nature of the narrow band waves near  $f_{cp(\text{local})}$  and its harmonics (Boardsen et al., 2015).

### 3.3. Waves in the Magnetosheath

Magnetosheath ULF waves have been extensively studied at Earth (e.g., Anderson et al., 1991; Gary et al., 1993; Lucek et al., 2005), but detailed investigation on the magnetosheath waves are limited at Mars

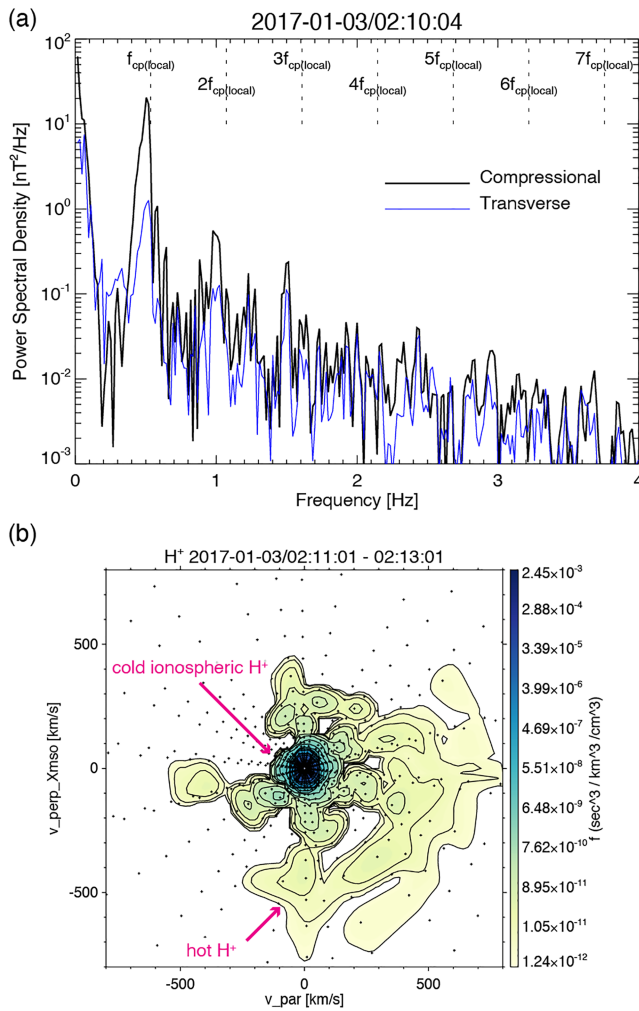


**Figure 4.** (a) Power spectra for compressional and transverse components obtained at the center time of 02:10:04 UT on 3 January 2017 (denoted by the vertical dotted line in Figure 3g). (b) Slice of the proton velocity distribution function on the  $v_{\parallel}$ - $v_{\perp}$  plane obtained during 02:11:01–02:13:01 UT on 3 January 2017 (denoted by the vertical dotted lines in Figure 3a). The black plus signs indicate the data points used to produce the contour plot.

Hz (Figure 8a), which is much higher than typical values of  $f_{cp(upstream)}$  (for the time interval used in this paper, the median and quartiles of the upstream magnetic field magnitude are 2.9, 2.1, and 4.3 nT, corresponding to  $f_{cp(upstream)}$  of 0.04, 0.03, and 0.07 Hz, respectively). The wave frequency is typically just below  $f_{cp(local)}$  (Figure 8b) with the median and quartiles of  $f/f_{cp(local)}$  of 0.80, 0.65, and 0.94. The wave power distribution exhibits at least two peaks, one at  $\sim 1$  nT<sup>2</sup>/Hz and another at  $\sim 100$  nT<sup>2</sup>/Hz (Figure 8c). As seen in Figure 8d, we obtain both compressional and transverse wave events.

Figure 9 shows the altitude-solar zenith angle (SZA) distributions of the wave properties. The magenta lines denote the nominal locations of the bow shock and MPB from Trotignon et al. (2006) as well as the optical shadow boundary ( $X_{MSO} < 0$  and  $\sqrt{Y_{MSO}^2 + Z_{MSO}^2} = R_M$ , where  $R_M$  is the Martian radius). The data density (the number of spectra in each bin) and the wave occurrence rate (the fraction of spectra in each bin containing narrow band waves) are shown in Figures 9a and 9b, respectively. The wave events are widely distributed with typical occurrence rates on the order of  $\sim 0.1$ –1%. The unnormalized wave frequency is high in the dayside MPR (Figure 9c), resulting from the enhanced intensity of the piled-up magnetic field. As seen in the normalized wave frequency distribution (Figure 9d),  $f/f_{cp(local)}$  is typically below 1 in the magnetosheath, while it can be close to 1 in the dayside MPR (except for the low altitudes  $< 300$  km) and in the nightside magnetotail. The total wave power (Figure 9e) and compressional to total power ratio (Figure 9f)

(Bertucci et al., 2004; Espley et al., 2004; Ruhunusiri et al., 2015). As reviewed by Dubinin and Fraenz (2016), complicated superposition of different modes from different sources is expected in the Martian magnetosheath. Here we briefly highlight properties of the detected narrow band  $f < \sim f_{cp(local)}$  waves, which have not been specifically investigated in the past literature on the Martian magnetosheath waves.

Figure 7 shows a transverse wave near and just below  $f_{cp(local)}$  observed in the Martian magnetosheath plasma. We observe narrow band peaks at  $\sim 0.5$ –0.8 Hz (Figure 7e) with predominantly transverse wave power (Figure 7f) at small propagation angles from the background magnetic field (Figure 7g) with left-handed polarization (Figure 7i). Consistent with these spectral features, the insert of Figure 7 displays a nearly sinusoidal waveform in each  $B_{MSO}$  component and smaller, irregular fluctuations in the magnetic field magnitude. The wave vector is almost perpendicular to the magnetosheath flow (Figure 7h), implying that the Doppler shift effect is minimal for the observed waves. For this event,  $f_{cp(upstream)}$  is estimated to be  $\sim 0.1$  Hz based on the interplanetary magnetic field magnitude of  $\sim 6.5$  nT measured at 16:50 UT just after the outbound bow shock crossing. At the times of wave detection, we observe moderate proton  $\beta$  of  $\sim 0.1$ –0.4 and high proton temperature anisotropy of  $\sim 2$ –4 (Figure 7b). These properties exhibit striking similarities to the electromagnetic proton cyclotron waves observed in the terrestrial magnetosheath (Anderson et al., 1991; Czaykowska et al., 2001).

## 4. Statistical Results

This section presents statistical properties of the detected waves and their association with local and upstream conditions. In total,  $\sim 45,000$  wave events (individual peaked spectra) were identified out of 11 million spectra by the procedure described in section 2, resulting in an overall occurrence rate of  $\sim 0.4\%$ .

### 4.1. Wave Properties

Figure 8 shows histograms of frequency and power properties of the narrow band waves detected by our algorithm. The vast majority of the detected narrow band waves have frequencies of  $\sim 0.1$ –1

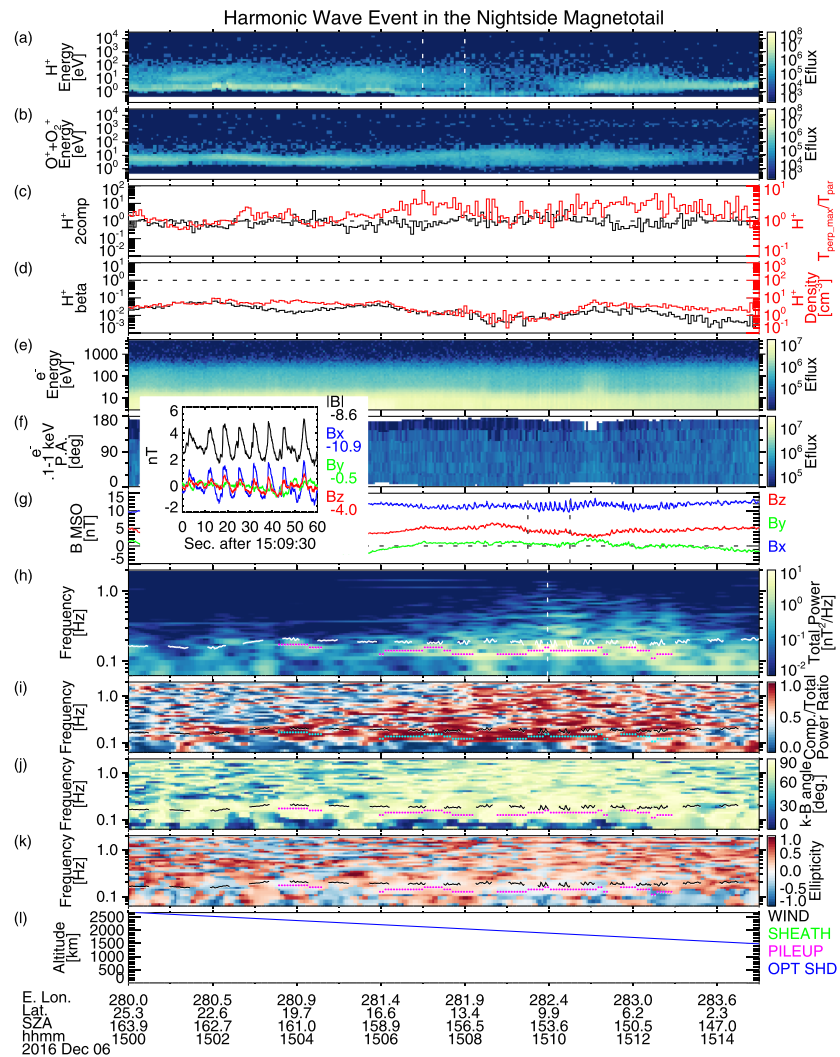


**Figure 5.** MAVEN observations during 15:00–15:15 UT on 6 December 2016. Figures 5a–5e and 5g–5l are in the same format as Figures 1a–1k. Figure 5f shows pitch angle distributions of 0.1–1 keV electrons.

are clearly organized by the nominal plasma regimes: strong ( $>10 \text{ nT}^2/\text{Hz}$ ), predominantly transverse waves in the magnetosheath; and weak ( $<10 \text{ nT}^2/\text{Hz}$ ), predominantly compressional waves in the dayside MPR and nightside magnetotail. Similarly, we typically observe small propagation angles with respect to the background magnetic field in the magnetosheath and nearly perpendicular propagation in the dayside MPR and nightside magnetotail (Figure 9g). The magnetosheath waves have preferentially left-handed polarization, while mixed polarities are seen below the MPB (Figure 9h). As the compressional and transverse waves exhibit distinctly different spatial distributions, we will show their properties separately in the following sections.

#### 4.2. Dependence on Local Plasma Conditions

We present altitude-SZA distributions of compressional and transverse wave occurrence in Figures 10a and 10b along with distributions of proton  $\beta$ , proton two-component parameter, and proton temperature anisotropy regardless of wave occurrence (Figures 10c, 10f, and 10i), at compressional wave occurrence (Figures 10d, 10g, and 10j), and at transverse wave occurrence (Figures 10e, 10h, and 10k). We note that the proton  $\beta$  discontinuity at the optical shadow boundary (Figure 10c) is caused by transition of spacecraft charging from positive potentials in the sunlit region to negative potentials in the shadow. The proton  $\beta$  in the sunlit MPR should be considered as a lower limit because a significant amount of low-energy protons could be repelled by the positive spacecraft potentials. Also, the limited field of view of STATIC can cause possible underestimations of the proton pressure up to  $\sim 30\%$  (Artemyev et al., 2017).

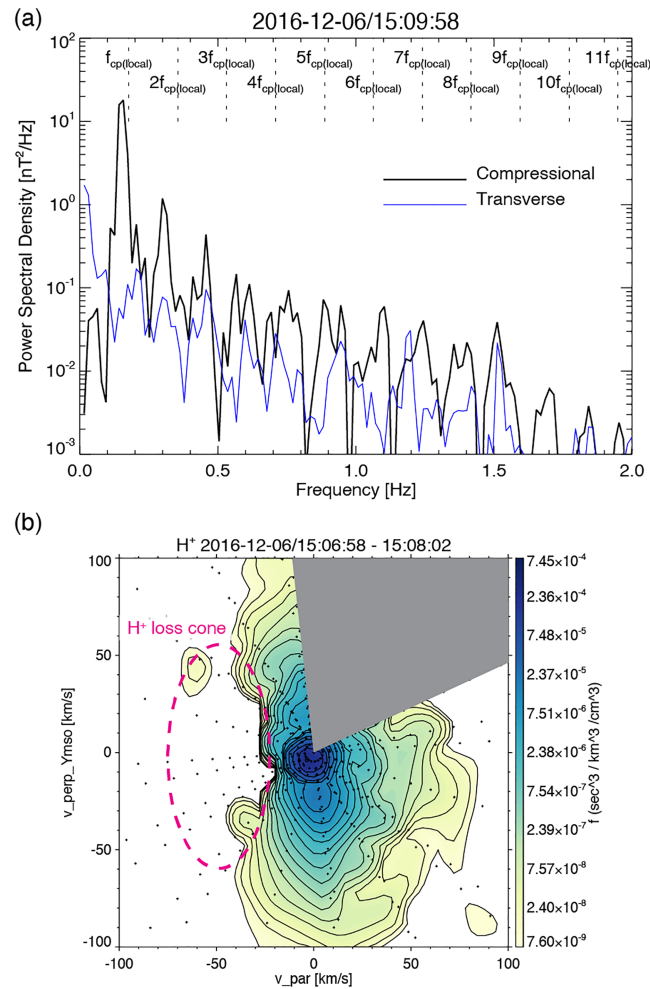


**Figure 6.** (a) Power spectra for compressional and transverse components obtained at the center time of 15:09:58 UT on 6 December 2016 (denoted by the vertical dotted line in Figures 5i and 5j). (b) Slice of the proton velocity distribution function on the  $v_{\parallel}$ - $v_{\perp Y_{M50}}$  plane obtained during 15:06:58-15:08:02 UT on 6 December 2016 (denoted by the vertical dotted lines in Figure 5a). The gray area displays the invisible directions outside of the unblocked STATIC field of view. The black plus signs indicate the data points used to produce the contour plot.

As illustrated and labeled in Figures 10a and 10b, several wave populations exemplified in Section 3 can be identified, including (i) compressional waves in the dayside MPR, (ii) predominantly compressional waves in the nightside magnetotail, and (iii) transverse waves in the magnetosheath. Each population exhibits characteristic local plasma conditions at wave detection:

(i) The compressional waves in the dayside MPR are associated with a relatively narrow range of low proton  $\beta$  (Figure 10d) compared to the nominal values (Figure 10c). Using measurements at altitudes of 200–800 km on the dayside (roughly corresponding to the population (i) region), quartile ranges of proton  $\beta$  are 0.0020–0.011 at compressional wave occurrence and 0.0011–0.068 for nominal conditions. The coexistence of hot and cold protons is strongly favored for the wave occurrence as seen by the high proton two-component parameters (Figure 10g) compared to the nominal values (Figure 10f). At altitudes of 200–800 km on the dayside, the proton two-component parameter exceeds 2 for 65% of the time at compressional wave occurrence, while this rate drops to 36% for nominal conditions. The proton temperature anisotropy at the wave occurrence (Figure 10j) is not much different from nominal conditions (Figure 10i).

(ii) The compressional waves in the nightside magnetotail are observed preferentially for low proton  $\beta$  (Figure 10d) compared to the nominal values (Figure 10c). At altitudes of 500–3,000 km in the optical shadow (roughly corresponding to the population (ii) region), quartile ranges of proton  $\beta$  are 0.0015–0.014

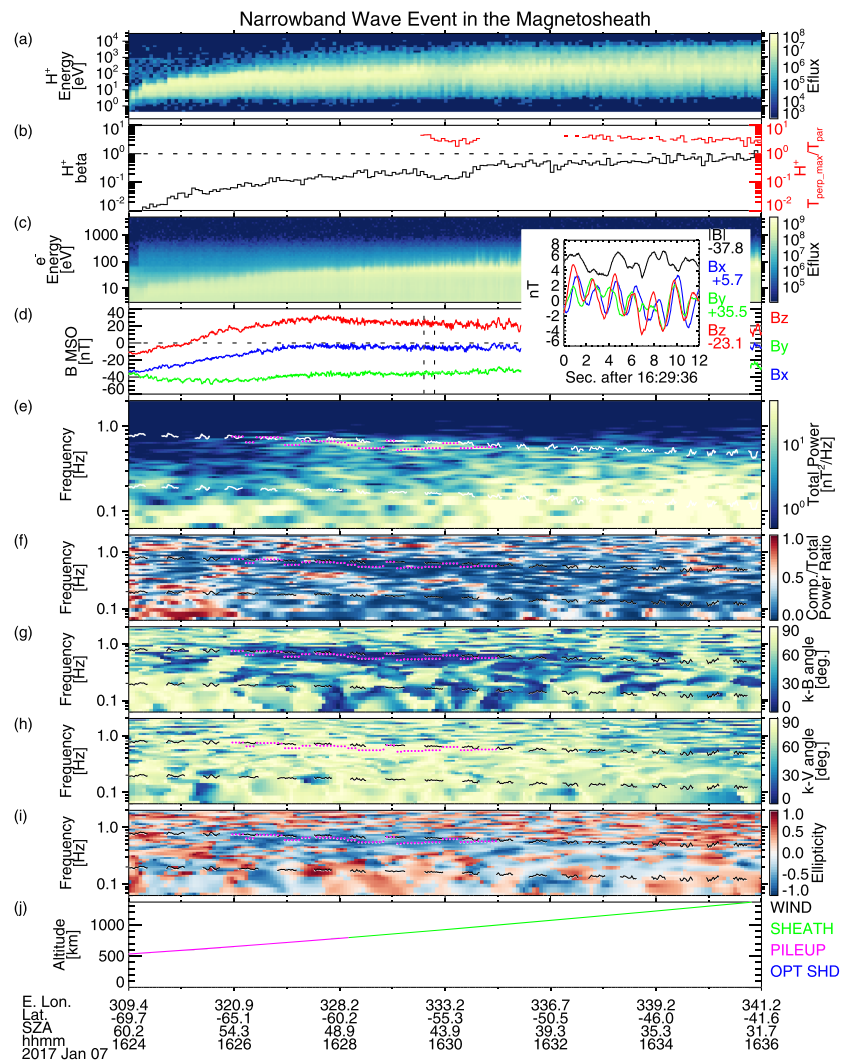


**Figure 7.** MAVEN observations during 16:24–16:36 UT on 7 January 2017 of (a)  $H^+$  energy spectra in units of differential energy flux (Eflux) of  $eV/cm^2/s/sr/eV$  obtained by STATIC, (b)  $H^+$   $\beta$  and temperature anisotropy, (c) electron energy spectra, (d) magnetic field in Mars Solar Orbital (MSO) coordinates, (e) magnetic field total wave power, (f) compressional to total power ratio, wave normal angle with respect to (g) the background magnetic field and (h) the magnetosheath flow (measured by SWIA), (i) ellipticity (+1 = right-handed circular polarization), and (j) spacecraft altitude color coded by nominal plasma regimes. The upper and lower dashed lines in Figures 7e–7i denote the local  $H^+$  and  $He^+$  cyclotron frequencies, respectively. The magenta dots in Figures 7e–7i indicate the narrow band waves identified by our selection algorithm. The insert shows the waveform during the time intervals indicated by the vertical dotted lines in Figure 7d.

at compressional wave occurrence and 0.0075–0.16 for nominal conditions. They are not particularly associated with two-component protons (Figure 10g). The proton temperature anisotropy (Figure 10j) is slightly higher than usual (Figure 10i) with quartile ranges of 1.1–3.3 at the wave occurrence and 0.91–2.1 for nominal conditions.

(iii) The transverse waves in the magnetosheath are closely associated with moderate proton  $\beta$  (Figure 10e), with no indication of two-component protons (Figure 10h), and with higher-than-usual proton temperature anisotropy particularly at low SZAs (Figure 10k). At altitudes below 3,000 km in the nominal magnetosheath region, quartile ranges of proton  $\beta$  are 0.28–1.2 at transverse wave occurrence and 1.4–10 for nominal conditions. Note that even well below the nominal MPB, these transverse waves are observed at relatively high rates (Figure 10b), coinciding with highly anisotropic, sheath-like protons (Figures 10e, 10h, and 10k) as is the case for the event shown in Figure 7.

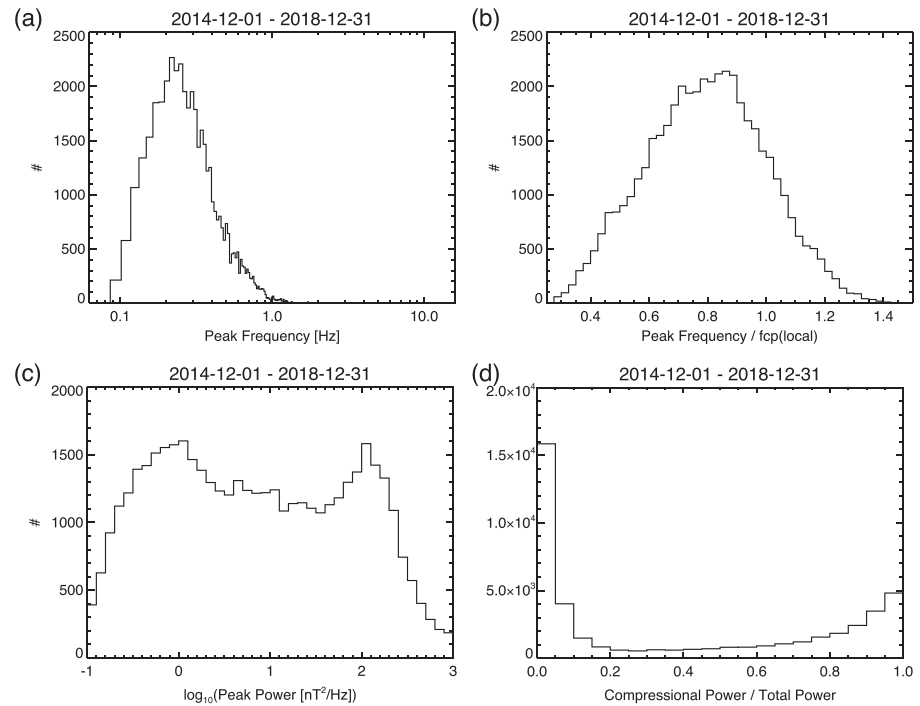


**Figure 8.** Histograms of (a) peak frequency, (b) peak frequency normalized by the local proton cyclotron frequency, (c) peak power, and (d) compressional to total power ratio of the detected waves.

Compressional waves observed at low occurrence rates near the bow shock (Figure 10a) exhibit local plasma conditions similar to those of population (iii). This implies that the separation of wave populations by the compressional to total power ratio of 0.5 may not be perfect and that a minor part of population (iii) could have significant compressional wave power. (Alternatively, there could be contamination of wave spectra at the bow shock.) Similarly, transverse waves that do not belong to the population (iii) (Figure 10b) are associated with local plasma conditions typical of populations (i) and (ii), suggesting that these waves may represent minor subsets of populations (i) and (ii) with transverse power exceeding compressional power.

### 4.3. Upstream Driver Control

Here we investigate solar wind and solar control of the wave occurrence. Figures 11a–11d show the compressional wave distributions divided into  $2 \times 2$  groups according to the solar wind dynamic pressure ( $P_{\text{dyn}}$ ) and solar EUV conditions, thereby distinguishing effects of solar wind and solar forcing. The top and bottom panels show low- and high- $P_{\text{dyn}}$  conditions, respectively. The panels on the left- and right-hand sides show low- and high-EUV conditions, respectively. For the compressional waves in the dayside upper ionosphere (population (i)), the wave occurrence is strongly controlled by the solar EUV as seen by the enhanced colors in Figures 11b and 11d compared to Figures 11a and 11c. Meanwhile, the difference between low (Figures 11a and 11b) and high  $P_{\text{dyn}}$  (Figures 11c and 11d) for population (i) is less pronounced, indicating that these waves are affected by the solar wind to a lesser extent. The compressional waves in the night-side magnetotail (population (ii)) show different dependence on the upstream conditions. Their occurrence depends on the combination of the  $P_{\text{dyn}}$  and EUV conditions, exhibiting high occurrence rates only for the high- $P_{\text{dyn}}$  and high-EUV case (Figure 11d) in stark contrast to the other cases (Figures 11a–11c). We note that the local occurrence rate of compressional waves can be as high as  $\sim 10\%$  under the favorable conditions, suggesting that these waves are not uncommon during high-EUV periods.

The  $P_{\text{dyn}}$  and EUV dependence of the transverse wave occurrence is shown in Figures 11e–11h. The population (iii) is observed at lower altitudes in the dayside MPR for high  $P_{\text{dyn}}$  conditions (Figures 11g and 11h) compared to low  $P_{\text{dyn}}$  conditions (Figures 11e and 11f), presumably resulting from the deeper penetration of sheath-like plasma and lower locations of the MPB. In contrast, the EUV dependence is less clear. Perhaps the most notable feature is the absence of transverse waves in the middle magnetosheath in Figure 11f.

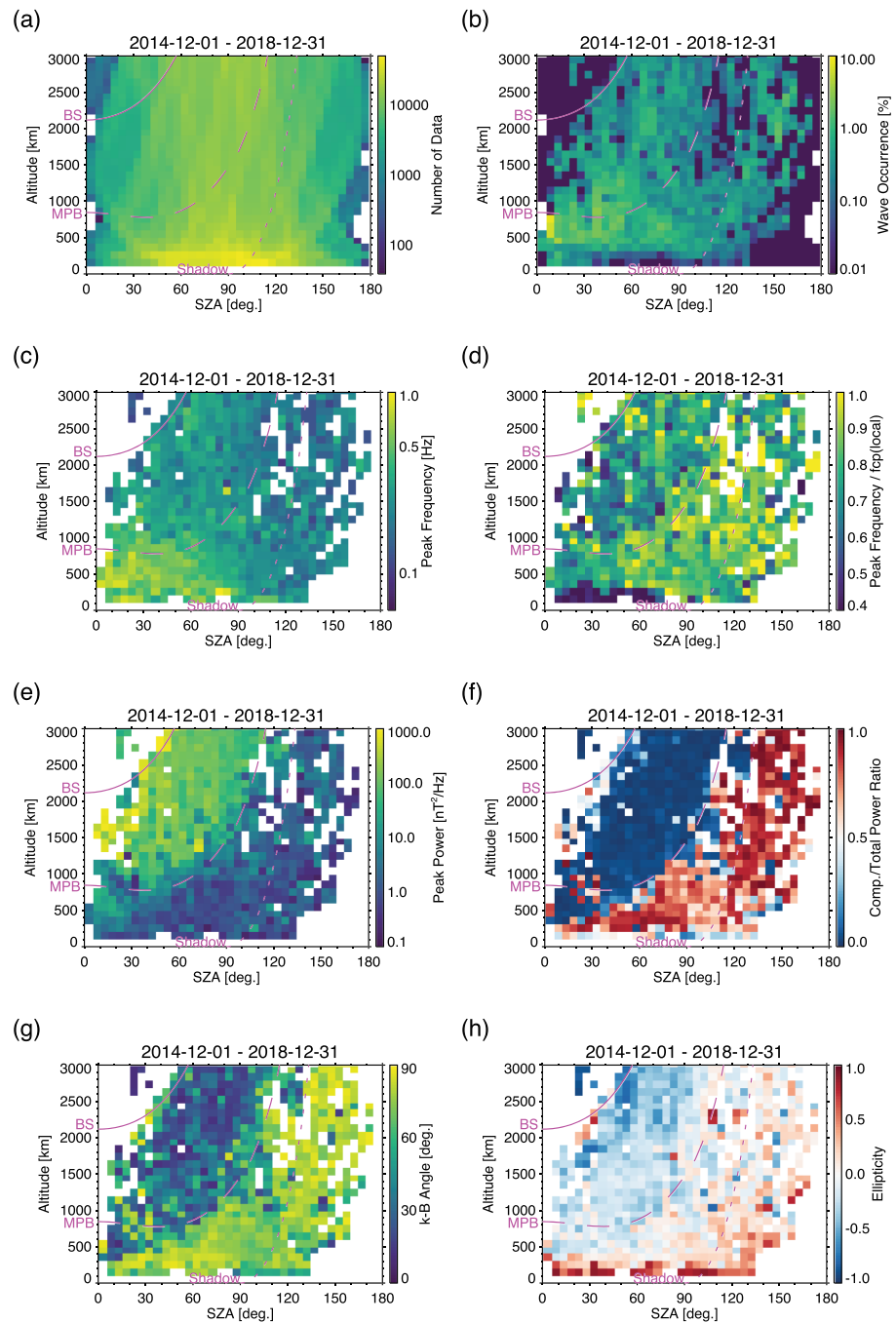


**Figure 9.** Altitude-solar zenith angle distributions of (a) data density, (b) wave occurrence, (c) median peak frequency, (d) median peak frequency normalized by the local proton cyclotron frequency, (e) median peak power, (f) median compressional to total power ratio, (g) median wave normal angle with respect to the background magnetic field, and (h) median wave ellipticity (positive = right handed). The magenta lines indicate the nominal locations of the bow shock, magnetic pileup boundary, and geometric shadow (Trotignon et al., 2006).

The transverse waves other than population (iii) behave in a similar manner to compressional populations (i) and (ii).

Next we investigate dependence of wave occurrence on magnetosheath properties, which are controlled by upstream solar wind drivers. As average magnetosheath properties depend strongly on upstream Mach numbers, we organize the wave distributions by separating them according to solar wind Alfvén Mach number ( $M_A$ ) conditions in Figures 12a–12d. The compressional waves below the MPB are not directly controlled

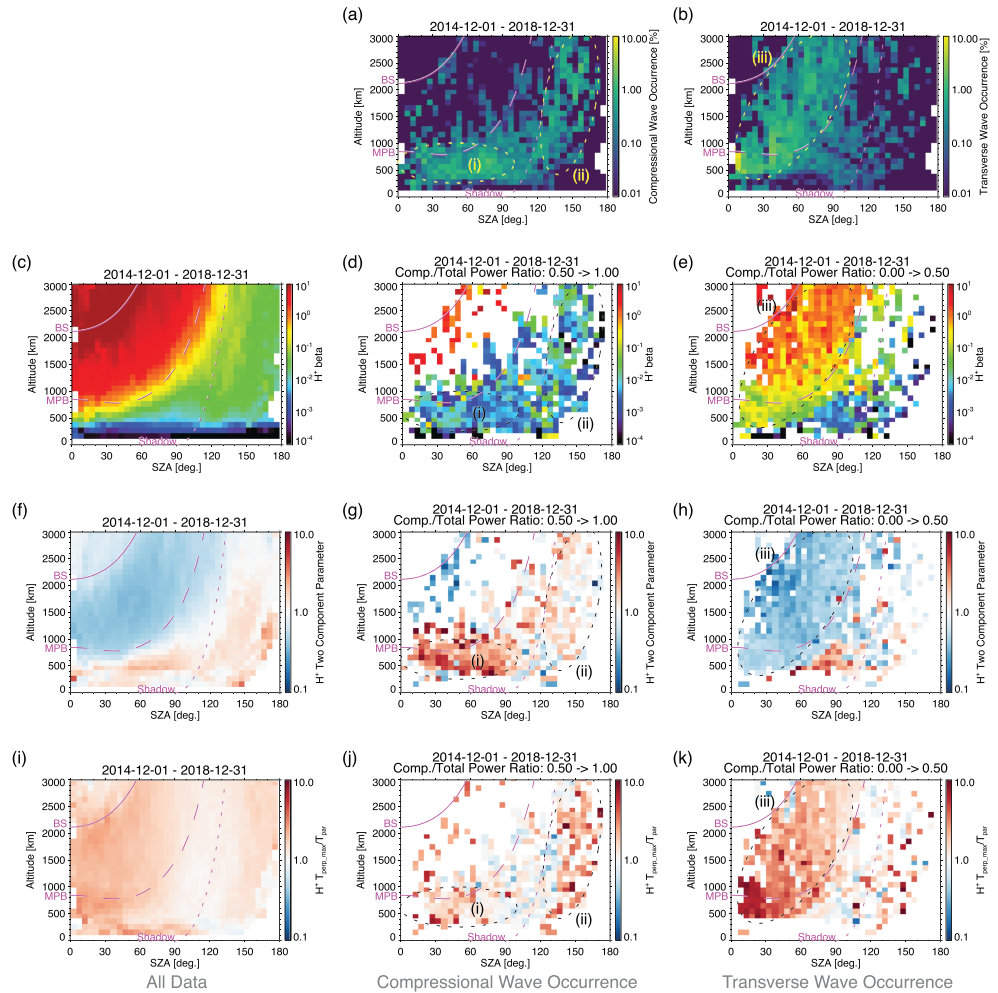


**Figure 10.** Altitude-solar zenith angle distributions of (a) compressional wave occurrence, (b) transverse wave occurrence, median proton  $\beta$  (c) of all data and when (d) compressional and (e) transverse waves are detected, median proton two-component parameter (f) of all data and when (g) compressional and (h) transverse waves are detected, and median proton temperature anisotropy (i) of all data and when (j) compressional and (k) transverse waves are detected. The dotted ovals with labels (i)–(iii) illustrate the different wave populations discussed in text.

by  $M_A$  (Figures 12a and 12b). The compressional waves in the dayside upper ionosphere (population (i)) exhibit little dependence on  $M_A$ . The compressional waves in the nightside magnetotail (population (ii)) show somewhat higher occurrence rates for low  $M_A$ , but the difference is not as distinct as that seen in Figure 11 organized by  $P_{\text{dyn}}$  and EUV (note that  $M_A$  and  $P_{\text{dyn}}$  are interrelated by the solar wind density and velocity). In contrast to the compressional waves, the transverse waves in the magnetosheath show pronounced dependence on  $M_A$ . The occurrence of transverse magnetosheath waves exhibits much higher rates for low  $M_A$  conditions as seen by the enhanced colors for population (iii) in Figure 12c compared to Figure 12d. We note that for low  $M_A$  conditions, average magnetosheath proton  $\beta$  is lower as expected from the stronger IMF strength and higher solar wind density and velocity, and proton temperature anisotropy is higher as reported from SWIA data by Halekas et al. (2017). Both of these trends were confirmed with STATIC data (not shown).

As magnetosheath properties depend also on whether the shock is quasi-parallel or quasi-perpendicular, we investigate dawn-dusk asymmetry of wave occurrence in Figures 12e and 12f. The solar zenith angles on the horizontal axis in Figures 12e and 12f are multiplied by signs of  $Y_{\text{MSO}}$  so that negative (positive) values correspond to the dawn (dusk) side. For nominal Parker spiral IMF configurations, the dawnside (duskside) bow shock corresponds to the quasi-parallel (quasi-perpendicular) shock. The compressional waves in the dayside upper ionosphere (population (i)) are observed preferentially on the dawn side (Figure 12e) with

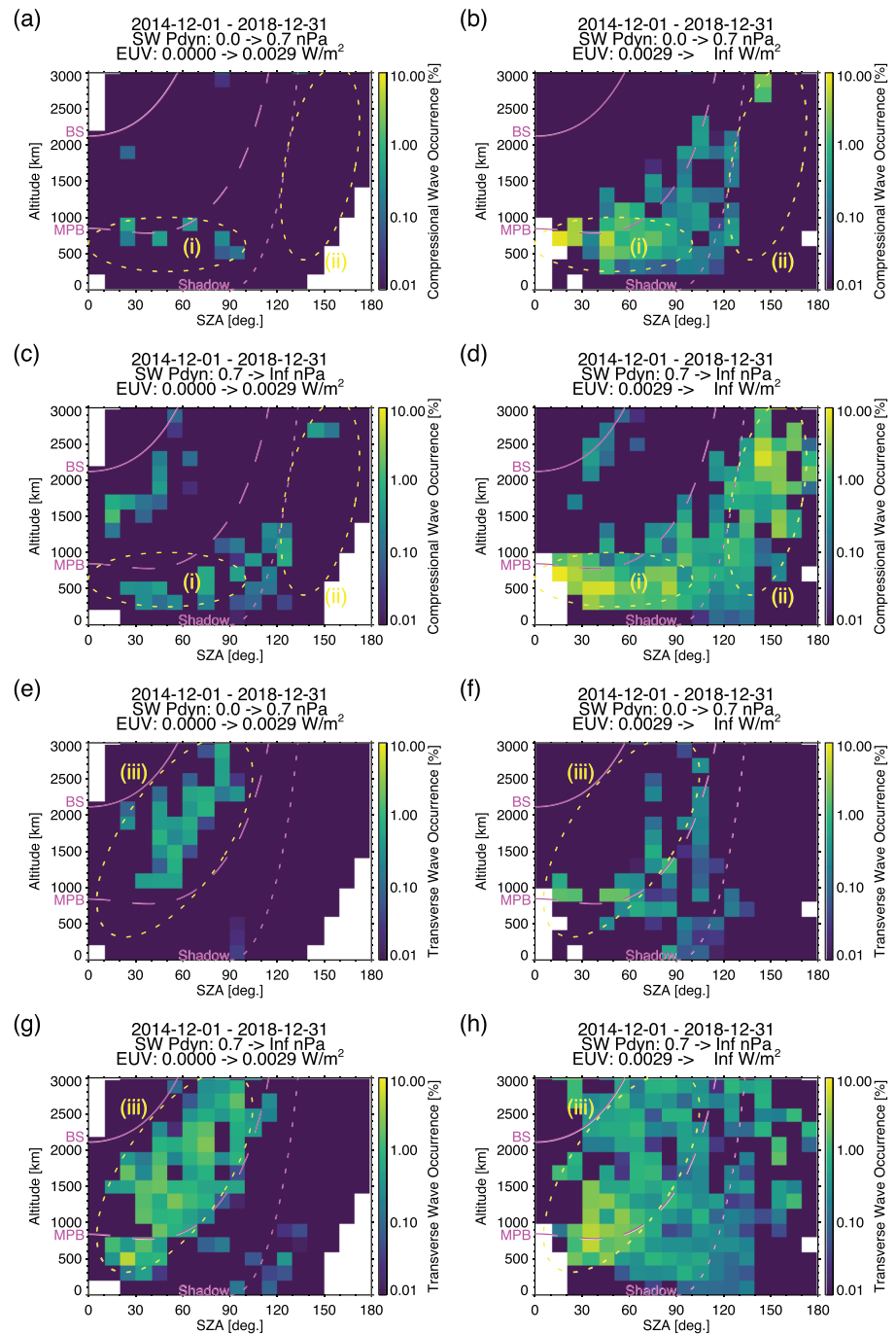


**Figure 11.** Altitude-solar zenith angle distributions of compressional wave occurrence for (a) low solar wind dynamic pressure ( $P_{\text{dyn}}$ ) and low solar extreme ultraviolet (EUV) conditions, (b) low  $P_{\text{dyn}}$  and high EUV conditions, (c) high  $P_{\text{dyn}}$  and low EUV conditions, (d) high  $P_{\text{dyn}}$  and high EUV conditions, and (e–h) transverse wave occurrence in the same format. The dotted ovals with labels (i)–(iii) illustrate the different wave populations discussed in text.

occurrence rates of 0.68% on the dawn side and 0.29% on the dusk side derived from the data obtained at altitudes of 200–800 km on the dayside. We could not identify any prominent dawn-dusk asymmetry for the compressional waves in the nightside magnetotail (population (ii); Figure 12e) with occurrence rates of 0.12% on the dawn side and 0.13% on the duskside derived from the data obtained at altitudes below 3000 km in the optical shadow. Figure 12f shows that the nominal quasi-perpendicular region on the dusk-side is favored for observations of the transverse waves (population (iii)) in the magnetosheath, though the

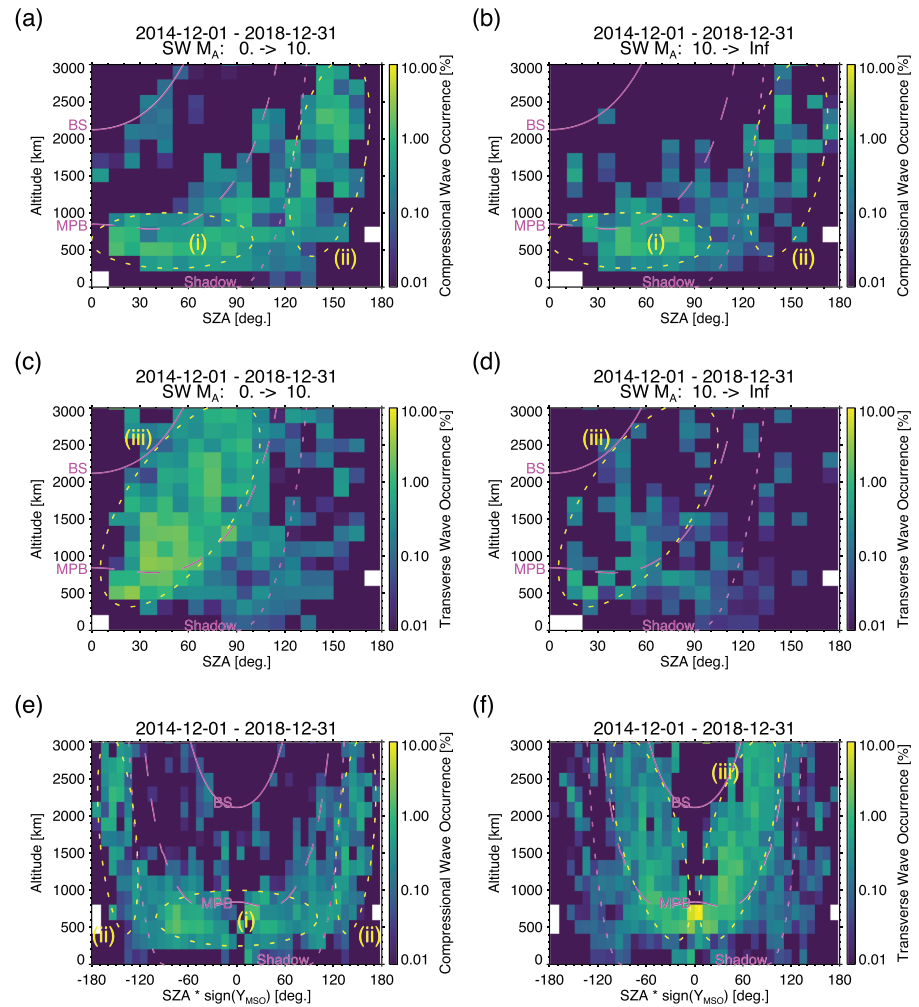


**Figure 12.** Altitude-solar zenith angle distributions of compressional wave occurrence for (a) low and (b) high solar wind Alfvén Mach number ( $M_A$ ) conditions, transverse wave occurrence for (c) low and (d) high  $M_A$  conditions, and (e) compressional and (f) transverse wave occurrence with the negative (positive) solar zenith angles corresponding to the dawn (dusk) side. The dotted ovals with labels (i)–(iii) illustrate the different wave populations discussed in text.

dawn-dusk asymmetry is less clear below the nominal MPB. We obtain transverse wave occurrence rates of 0.32% on the dawnside and 0.55% on the duskside from the data obtained at altitudes below 3,000 km in the nominal magnetosheath region. We note that higher proton temperature anisotropy is observed by SWIA in the quasi-perpendicular magnetosheath (Halekas et al., 2017), and we obtained similar results from STATIC data (not shown).

## 5. Discussion

### 5.1. Summary of Observations

The observed properties of narrow band magnetic field fluctuations near  $f_{cp(local)}$  (which is typically much higher than  $f_{cp(upstream)}$ ) below the Martian bow shock are summarized as follows:

1. In the dayside upper ionosphere, compressional waves are observed preferentially for a relatively narrow range of low proton  $\beta$  on the order of  $\sim 0.001$ – $0.01$ , for high solar EUV conditions, on the dawnside, and in the presence of two distinct components of hot and cold protons. The hot proton component in the MPR can be partly explained by perpendicular entry of gyrating magnetosheath protons, but there could be contribution from more complex entry mechanisms in inhomogeneous magnetic field geometry deviated from a smooth draped field. Sometimes harmonic structures are observed above  $f_{cp(local)}$ .
2. In the nightside magnetotail, compressional waves are observed preferentially for low proton  $\beta$  of  $\sim 0.001$ – $0.01$  under high-solar-EUV, strong-solar-wind conditions. These waves are accompanied not

necessarily by two-component protons but sometimes by warm, anisotropic protons with large loss cones. Sometimes harmonic structures are observed above  $f_{cp(local)}$ .

3. Transverse, left-hand polarized waves with frequencies typically below  $f_{cp(local)}$  propagating at small angles from the background magnetic field are observed preferentially in the duskside magnetosheath (nominal quasi-perpendicular region), with high proton temperature anisotropy, and for moderate local proton  $\beta$  of  $\sim 0.1$ – $1$  under low solar wind Mach number conditions. These waves are also observed below the nominal MPB along with magnetosheath-like protons.

### 5.2. Sources of the Compressional Waves in the Dayside Upper Ionosphere

First we consider sources of the compressional waves in the dayside upper ionosphere (population (i)). The close association of wave occurrence with the coexistence of distinct hot and cold proton components suggests that the hot protons of magnetosheath origin and cold ionospheric protons jointly form proton VDFs unstable to the generation of these waves. As exemplified in Figures 2 and 4b, injection of hot, ring/shell-like protons can lead to  $\partial f_p(v_{\perp})/\partial v_{\perp} > 0$ , which can be unstable to a proton Bernstein mode instability (e.g., Gary et al., 2011). The proton Bernstein mode instability can explain the narrow band spectral peaks near  $f_{cp(local)}$  and its harmonics, nearly perpendicular propagation, and compressional nature of the waves (Boardsen et al., 2012, 2015; Gary et al., 2010, 2011; Perraut et al., 1982). Instability analyses for terrestrial “magnetosonic waves” indicate that the speed of ring protons ( $V_R$ ) must exceed the Alfvén speed for the generation of low harmonic ( $f < 10f_{cp(local)}$ ) waves (Chen et al., 2010; Horne et al., 2000; Perraut et al., 1982). For the time intervals of Figures 2 and 4b, we obtain the proton Alfvén speed ( $V_{Ap}$ ) of 226 and 224 km/s, respectively. Therefore, we indeed confirm that  $V_R$  of the hot proton component (several hundreds of kilometers per second; see Figures 2 and 4b) substantially exceeds  $V_{Ap}$  for both cases. We point out that in contrast to the terrestrial magnetosonic waves that are typically confined close to the magnetic equator (however, see Broughton et al., 2008; Engebretson et al., 2010), the detected compressional waves are widely distributed around Mars presumably resulting from the similarly distributed ring/shell-like protons (Figure 10g).

The requirement of  $V_R$  exceeding  $V_{Ap}$  could explain the prominent EUV dependence of the  $f \sim f_{cp(local)}$  wave occurrence. Figure 13 shows  $P_{dyn}$ -EUV dependence of  $V_{Ap}$ . In the dayside upper ionosphere,  $V_{Ap}$  is much lower for high EUV conditions (Figures 13b and 13d) compared to that for low EUV conditions (Figures 13a and 13c) because of higher ionospheric proton density under high solar EUV irradiation. Considering that hot protons of magnetosheath origin typically have  $V_R$  of several hundred kilometers per second, the high  $V_{Ap}$  comparable to or exceeding these speeds for low EUV conditions (Figures 13a and 13c) could inhibit the generation of low harmonic waves even in the presence of ring-like protons. We note that the proton Alfvén speed is slightly higher for high  $P_{dyn}$  conditions because of the enhanced magnetic field intensity imposed by stronger compression, but the proton density variation by EUV has a larger impact on the  $V_{Ap}$  variability.

The dawn-dusk asymmetry of the wave occurrence could be caused by asymmetric access of solar wind protons to the upper ionosphere, asymmetric proton density profiles in the upper ionosphere, or both. On the dawnside downstream of the nominal quasi-parallel shock, the magnetic field geometry is more complicated, and the solar wind plasma tends to penetrate deeper into the Martian magnetosphere (Diéval et al., 2012; Dubinin et al., 2008). Additionally, dawn-dusk asymmetry in the local proton density (which could result from diurnal variations in the neutral hydrogen density; e.g., Chaufray et al., 2015) may lead to asymmetric wave generation because of the  $V_R > V_{Ap}$  requirement. From the data obtained at altitudes of 200–800 km on the dayside, occurrence rates of proton two-component parameters exceeding 2 are 37% on the dawnside and 34% on the duskside, and median proton densities are  $3.2 \text{ cm}^{-3}$  on the dawnside and  $2.1 \text{ cm}^{-3}$  on the duskside, resulting in median  $V_{Ap}$  of 358 km/s on the dawnside and 422 km/s on the duskside. Both of these trends are qualitatively consistent with the observed preference for the dawnside.

The preference for a relatively narrow range of proton  $\beta$  could be attributed to the property of the proton Bernstein mode instability (Gary et al., 2010, 2011). The growth rate of the proton Bernstein mode instability is not a monotonic function of proton  $\beta$ , but it has a peak at a certain value of proton  $\beta$ ,  $\sim 0.5$  for the parameters used by Gary et al. (2010) and thermal proton  $\beta$  of  $\sim 0.1$  for the case of Gary et al. (2011). Neither of these proton  $\beta$  values is directly applicable to the Martian upper ionosphere because cold, dense ionospheric protons are not included in these studies. Gary et al. (2010) considered a proton VDF without a cold component, and Gary et al. (2011) assumed a hot to total density ratio of 0.35 in contrast to the corresponding ratios of  $< \sim 0.01$  in our cases (we obtain hot [ $> 50 \text{ eV}$ ] to total density ratios of  $5 \times 10^{-3}$  and  $6 \times 10^{-4}$  for the

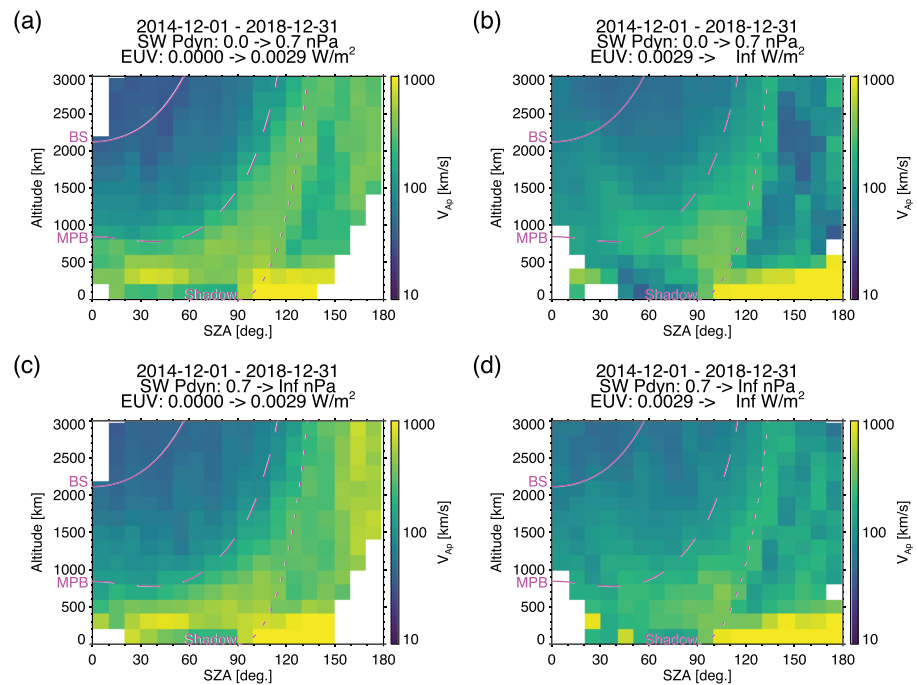


**Figure 13.** Altitude-solar zenith angle distributions of the proton Alfvén speed ( $V_{Ap}$ ) for (a) low solar wind dynamic pressure ( $P_{dyn}$ ) and low solar extreme ultraviolet (EUV) conditions, (b) low  $P_{dyn}$  and high EUV conditions, (c) high  $P_{dyn}$  and low EUV conditions, and (d) high  $P_{dyn}$  and high EUV conditions.

time intervals of Figures 2 and 4b). Instability analysis with appropriate parameters and proton VDFs representative of the Martian upper ionosphere would be necessary to establish the causal relationship between the observed waves and two-component protons, but such studies are beyond the scope of the paper.

### 5.3. Sources of the Compressional Waves in the Nightside Magnetotail

The lack of clear association of the nightside compressional waves (population (ii)) with two-component protons suggests that we need to seek for energy sources other than the hot, ring-like protons. Proton loss cone distributions provide a plausible candidate. As demonstrated in Figure 6b, large proton loss cones are observed together with compressional waves for some cases. In this sense, the compressional narrow band emissions in the Martian magnetotail have notable similarities to those in Mercury's inner magnetosphere (Boardsen et al., 2012, 2015). Boardsen et al. (2012, 2015) attribute the wave generation to a proton Bernstein mode instability driven by a positive perpendicular slope near the edge of a large proton loss cone. Meanwhile, major differences of their results from our observations include that cold, dense ionospheric protons do not exist at Mercury and that the compressional waves are generated in the high proton  $\beta$  region near the magnetic equator in the Mercury's magnetosphere.

The common presence of electron loss cones in the Martian magnetotail (e.g., Brain et al., 2007; Harada et al., 2016; Lillis et al., 2004; Weber et al., 2017) suggests that proton loss cones will be also formed if external warm protons are supplied along open field lines from the magnetosheath (note that a source cone will be formed by cold protons directly supplied from the ionosphere). The warm proton flux in the magnetotail is strongly controlled by  $P_{dyn}$  (Harada et al., 2015), which could explain the requirement of high  $P_{dyn}$  for wave occurrence. The prominent EUV dependence of wave occurrence suggests that the presence of cold, dense ionospheric protons is another necessary condition for the wave generation. The resulting lower  $V_{Ap}$  in the magnetotail (Figures 13b and 13d) leads to lower phase speeds, which may represent a favorable condition for the excitation of low harmonic waves (Chen et al., 2010). The preference for low proton  $\beta$  of  $\sim 0.001$ – $0.01$ , which is similar to that for population (i), could reflect the property of the proton Bernstein mode instability as discussed in section 5.2.

### 5.4. Sources of the Magnetosheath Waves

As is well established for terrestrial magnetosheath waves, proton  $\beta$  controls the nature of local wave generation driven by proton temperature anisotropy. For moderate proton  $\beta < \sim 1$ , transverse electromagnetic

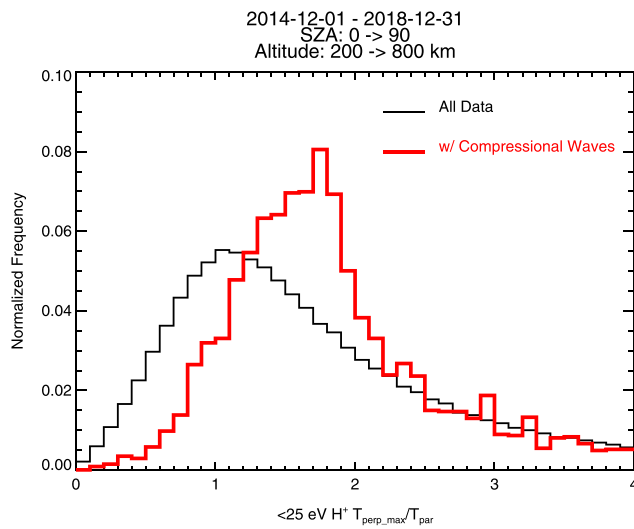


**Figure 14.** Histograms of low-energy (<25 eV) proton temperature anisotropy in the dayside upper ionosphere from all data (black) and at compressional wave occurrence (red).

proton cyclotron waves are expected to be generated through the proton cyclotron instabilities, while the mirror mode instabilities tend to dominate for high proton  $\beta$  (e.g., Czaykowska et al., 2001; Gary et al., 1993; Lucek et al., 2005). The transverse waves observed in the Martian magnetosheath indeed exhibit generally left-handed polarizations, small propagation angles with respect to the background magnetic field, and preference for moderate proton  $\beta \sim 0.1$ –1 resulting from low solar wind  $M_A$ . The transverse waves are observed preferentially in the nominal quasi-perpendicular (dusk) region, where higher proton temperature anisotropy is observed (Halekas et al., 2017). These properties are all consistent with electromagnetic proton cyclotron waves driven by proton temperature anisotropy. The lower wave occurrence for high EUV conditions (Figure 11f) could be attributed to the addition of heavy ions of planetary origin as pointed out by Dubinin and Fraenz (2016) because higher density ratios of heavy ions to protons can reduce the growth rate of the proton cyclotron instability (Gary et al., 1993). Espley et al. (2004) reported Mars Global Surveyor observations of ion cyclotron waves in the nightside magnetosheath. In contrast, the MAVEN observations presented here demonstrate that proton cyclotron waves can be generated in the dayside magnetosheath and even well below the nominal MPB location. As mirror mode oscillations are observed at frequencies well below

$f_{cp(local)}$  (Bertucci et al., 2004; Espley et al., 2004; Ruhunusiri et al., 2015), they would not be detected by our algorithm. The absence of narrow band wave detection near  $f_{cp(local)}$  for high  $M_A$  conditions (Figure 12) could result from preferential excitation of the mirror mode instabilities.

### 5.5. Effects of the Compressional Waves in the Dayside Upper Ionosphere

The proton Bernstein mode waves can cause perpendicular heating of thermal protons via cyclotron resonant absorption, thereby depositing energy to them (Horne et al., 2000). To investigate the possible effect of perpendicular heating on ionospheric protons, we compute proton temperature anisotropy with a limited energy range (<25 eV) from STATIC data. Figure 14 compares histograms of the low-energy proton temperature anisotropy obtained at 200–800 km altitudes on the dayside for overall distributions (black) and at compressional wave occurrence (red). We observe that the distribution of low-energy proton anisotropy shifts toward high values when the compressional waves is detected, implying that the higher-than-usual anisotropy results from perpendicular heating of thermal protons by proton Bernstein mode waves. If true, the wave-particle interaction facilitates energy transfer from precipitating hot protons to local ionospheric protons without direct collisions between particles. This represents another pathway of energy flows from the solar wind to the upper ionosphere, albeit with small overall contribution to atmospheric heating (e.g., Diéval et al., 2013).

## 6. Conclusions

The MAVEN observations of narrow band magnetic field fluctuations near  $f_{cp(local)}$  below the Martian bow shock reveal newly identified wave populations of compressional narrow band emissions in the dayside upper ionosphere and in the nightside magnetotail. High solar EUV conditions are particularly favored for the occurrence of the dayside waves, and high solar wind dynamic pressures are additionally favored for the occurrence of the nightside waves. The properties of the waves and their dependence on local and upstream conditions can be generally explained by a proton Bernstein mode instability driven by a positive perpendicular slope in proton VDFs. In the dayside upper ionosphere, the free energy is provided presumably by ring/shell-like, hot protons of magnetosheath origin precipitating into cold, dense protons of ionospheric origin. In the nightside magnetotail, large loss cones of warm protons could be unstable to the proton Bernstein mode instability. Additionally, the MAVEN observations in the magnetosheath confirm the expected presence of electromagnetic proton cyclotron waves driven by proton temperature anisotropy in a moderate  $\beta$  plasma. Low solar wind Mach numbers are favored for the occurrence of these waves. The dayside proton Bernstein mode waves can cause perpendicular heating of thermal protons in the upper ionosphere.

**Acknowledgments**

This work was partially supported by the MAVEN project and the French space agency CNES. This work was supported by JSPS KAKENHI Grant JP19K14784. S. O. is supported by Japan Society for the Promotion of Science (JSPS) (19J14368). K. Y. is supported by Japan Society for the Promotion of Science (JSPS) (19J14222). MAVEN data are publicly available through the Planetary Data System (at <https://pds-ppi.igpp.ucla.edu>).

**References**

Anderson, B. J., Fuselier, S. A., & Murr, D. (1991). Electromagnetic ion cyclotron waves observed in the plasma depletion layer. *Geophysical Research Letters*, *18*(11), 1955–1958. <https://doi.org/10.1029/91GL02238>

Artemyev, A. V., Angelopoulos, V., Halekas, J. S., Runov, A., Zelenyi, L. M., & McFadden, J. P. (2017). Mars's magnetotail: Nature's current sheet laboratory. *Journal of Geophysical Research: Space Physics*, *122*, 5404–5417. <https://doi.org/10.1002/2017JA024078>

Bertucci, C., Mazelle, C., Crider, D. H., Mitchell, D. L., Sauer, K., Acuña, M. H., et al. (2004). MGS MAG/ER observations at the magnetic pileup boundary of Mars: draping enhancement and low frequency waves. *Advances in Space Research*, *33*(11), 1938–1944. <https://doi.org/10.1016/j.asr.2003.04.054>

Boardsen, S. A., Kim, E.-H., Raines, J. M., Slavin, J. A., Gershman, D. J., Anderson, B. J., & Travnicek, P. (2015). Interpreting ~1 Hz magnetic compressional waves in Mercury's inner magnetosphere in terms of propagating ion-Bernstein waves. *Journal of Geophysical Research: Space Physics*, *120*, 4213–4228. <https://doi.org/10.1002/2014JA020910>

Boardsen, S. A., Slavin, J. A., Anderson, B. J., Korth, H., Schriver, D., & Solomon, S. C. (2012). Survey of coherent similar to 1 Hz waves in Mercury's inner magnetosphere from MESSENGER observations. *Journal of Geophysical Research*, *117*, A00M05. <https://doi.org/10.1029/2012JA017822>

Brain, D. A., Bagenal, F., Acuña, M. H., Connerney, J. E. P., Crider, D. H., Mazelle, C., et al. (2002). Observations of low-frequency electromagnetic plasma waves upstream from the Martian shock. *Journal of Geophysical Research*, *107*(A6), 1076. <https://doi.org/10.1029/2000JA000416>

Brain, D. A., Lillis, R. J., Mitchell, D. L., Halekas, J. S., & Lin, R. P. (2007). Electron pitch angle distributions as indicators of magnetic field topology near Mars. *Journal of Geophysical Research*, *112*, A09201. <https://doi.org/10.1029/2007JA012435>

Broughton, M. C., Engebretson, M. J., Glassmeier, K. H., Narita, Y., Keiling, A., Fornaçon, K. H., et al. (2008). Ultra-low-frequency waves and associated wave vectors observed in the plasma sheet boundary layer by Cluster. *Journal of Geophysical Research*, *113*, A12217. <https://doi.org/10.1029/2008JA013366>

Chaufray, J.-Y., Gonzalez-Galindo, F., Forget, F., Lopez-Valverde, M., Leblanc, F., Modolo, R., & Hess, S. (2015). Variability of the hydrogen in the martian upper atmosphere as simulated by a 3D atmosphere-exosphere coupling. *Icarus*, *245*, 282–294. <https://doi.org/10.1016/j.icarus.2014.08.038>

Chen, L., Thorne, R. M., Jordanova, V. K., & Horne, R. B. (2010). Global simulation of magnetosonic wave instability in the storm time magnetosphere. *Journal of Geophysical Research*, *115*, A11222. <https://doi.org/10.1029/2010JA015707>

Collinson, G., Wilson, L. B., Omidi, N., Sibeck, D., Espley, J., Fowler, C. M., et al. (2018). Solar Wind induced waves in the skies of Mars: Ionospheric compression, energization, and escape resulting from the impact of ultra-low frequency magnetosonic waves generated upstream of the Martian bow shock. *Journal of Geophysical Research: Space Physics*, *123*, 7241–7256. <https://doi.org/10.1029/2018JA025414>

Connerney, J., Espley, J., Lawton, P., Murphy, S., Odom, J., Oliverson, R., & Sheppard, D. (2015). The MAVEN Magnetic Field Investigation. *Space Science Reviews*, *195*, 257–291. <https://doi.org/10.1007/s11214-015-0169-4>

Czaykowska, A., Bauer, T. M., Treumann, R. A., & Baumjohann, W. (2001). Magnetic field fluctuations across the Earth's bow shock. *Annales Geophysicae*, *19*(3), 275–287. <https://doi.org/10.5194/angeo-19-275-2001>

DiBaccio, G. A., Luhmann, J. G., Curry, S. M., Espley, J. R., Xu, S., Mitchell, D. L., et al. (2018). The twisted configuration of the Martian magnetotail: MAVEN observations. *Geophysical Research Letters*, *45*, 4559–4568. <https://doi.org/10.1029/2018GL077251>

Diéval, C., Kallio, E., Stenberg, G., Barabash, S., & Jarvinen, R. (2012). Hybrid simulations of proton precipitation patterns onto the upper atmosphere of Mars. *Earth, Planets and Space*, *64*(2), 121–134. <https://doi.org/10.5047/eps.2011.08.015>

Diéval, C., Stenberg, G., Nilsson, H., & Barabash, S. (2013). A statistical study of proton precipitation onto the Martian upper atmosphere: Mars Express observations. *Journal of Geophysical Research: Space Physics*, *118*, 1972–1983. <https://doi.org/10.1002/jgra.50229>

Dubinin, E., Chanteur, G., Fraenz, M., Modolo, R., Woch, J., Roussos, E., & Winningham, J. (2008). Asymmetry of plasma fluxes at Mars. ASPERA-3 observations and hybrid simulations. *Planetary and Space Science*, *56*(6), 832–835. <https://doi.org/10.1016/j.pss.2007.12.006>

Dubinin, E., & Fraenz, M. (2016). Ultra-low-frequency waves at Venus and Mars. In A. Keiling, D. H. Lee, & V. Nakariakov (Eds.), *Low-Frequency Waves in Space Plasmas* pp. 343–364. Hoboken, NJ: John Wiley Inc. <https://doi.org/10.1002/9781119055006.ch20>

Dubinin, E., Fraenz, M., Fedorov, A., Lundin, R., Edberg, N., Duru, F., & Vaisberg, O. (2012). Ion energization and escape on Mars and Venus. *Space Science Reviews*, *162*, 173–211. [https://doi.org/10.1007/978-1-4614-3290-6\\_6](https://doi.org/10.1007/978-1-4614-3290-6_6)

Dubinin, E., Fraenz, M., Pätzold, M., McFadden, J., Mahaffy, P. R., Eparvier, F., et al. (2017). Effects of solar irradiance on the upper ionosphere and oxygen ion escape at Mars: MAVEN observations. *Journal of Geophysical Research: Space Physics*, *122*, 7142–7152. <https://doi.org/10.1002/2017JA024126>

Engebretson, M. J., Kahlstorf, C. R. G., Posch, J. L., Keiling, A., Walsh, A. P., Denton, R. E., et al. (2010). Multiple harmonic ULF waves in the plasma sheet boundary layer observed by Cluster. *Journal of Geophysical Research*, *115*, A12225. <https://doi.org/10.1029/2010JA015929>

Eparvier, F. G., Chamberlin, P. C., Woods, T. N., & Thiemann, E. M. B. (2015). The solar extreme ultraviolet monitor for MAVEN. *Space Science Reviews*, *195*(1), 293–301. <https://doi.org/10.1007/s11214-015-0195-2>

Espley, J. R. (2018). The Martian magnetosphere: Areas of unsettled terminology. *Journal of Geophysical Research: Space Physics*, *123*, 4521–4525. <https://doi.org/10.1029/2018JA025278>

Espley, J. R., Cloutier, P. A., Brain, D. A., Crider, D. H., & Acuña, M. H. (2004). Observations of Low-Frequency Magnetic Oscillations in the Martian Magnetosheath, Magnetic Pileup Region, and Tail. *Journal of Geophysical Research*, *109*, A07213. <https://doi.org/10.1029/2003JA010193>

Fowler, C. M., Andersson, L., Ergun, R. E., Harada, Y., Hara, T., Collinson, G., et al. (2018). MAVEN observations of solar wind-driven magnetosonic waves heating the Martian dayside ionosphere. *Journal of Geophysical Research: Space Physics*, *123*, 4129–4149. <https://doi.org/10.1029/2018JA025208>

Fowler, C. M., Ergun, R. E., Andersson, L., Peterson, W. K., Hara, T., McFadden, J., et al. (2017). Ion heating in the Martian ionosphere. *Journal of Geophysical Research: Space Physics*, *122*, 10,612–10,625. <https://doi.org/10.1002/2017JA024578>

Gary, S. P., Fuselier, S. A., & Anderson, B. J. (1993). Ion anisotropy instabilities in the magnetosheath. *Journal of Geophysical Research*, *98*(A2), 1481–1488. <https://doi.org/10.1029/92JA01844>

Gary, S. P., Liu, K., & Winske, D. (2011). Bernstein instability driven by suprathermal protons in the ring current. *Journal of Geophysical Research*, *116*, A08215. <https://doi.org/10.1029/2011JA016543>

Gary, S. P., Liu, K., Winske, D., & Denton, R. E. (2010). Ion Bernstein instability in the terrestrial magnetosphere: Linear dispersion theory. *Journal of Geophysical Research*, *115*, A12209. <https://doi.org/10.1029/2010JA015965>

Gurnett, D. A. (1976). Plasma wave interactions with energetic ions near the magnetic equator. *Journal of Geophysical Research*, *81*(16), 2765–2770. <https://doi.org/10.1029/JA081i016p02765>

- Halekas, J. S., Brain, D. A., Luhmann, J. G., DiBraccio, G. A., Ruhunusiri, S., Harada, Y., et al. (2017). Flows, fields, and forces in the Mars-solar wind interaction. *Journal of Geophysical Research: Space Physics*, *122*, 11,320–11,341. <https://doi.org/10.1002/2017JA024772>
- Halekas, J. S., McFadden, J. P., Connerney, J. E. P., Espley, J. R., Brain, D. A., Mitchell, D. L., et al. (2015). Time-dispersed ion signatures observed in the Martian magnetosphere by MAVEN. *Geophysical Research Letters*, *42*, 8910–8916. <https://doi.org/10.1002/2015GL064781>
- Halekas, J. S., Ruhunusiri, S., Harada, Y., Collinson, G., Mitchell, D. L., Mazelle, C., et al. (2016). Structure, dynamics, and seasonal variability of the Mars-solar wind interaction: MAVEN solar wind ion analyzer inflight performance and science results. *Journal of Geophysical Research: Space Physics*, *121*, 547–578. <https://doi.org/10.1002/2016JA023167>
- Halekas, J. S., Taylor, E. R., Dalton, G., Johnson, G., Curtis, D. W., McFadden, J. P., et al. (2015). The solar wind ion analyzer for MAVEN. *Space Science Reviews*, *195*, 125–151. <https://doi.org/10.1007/s11214-013-0029-z>
- Harada, Y., Andersson, L., Fowler, C. M., Mitchell, D. L., Halekas, J. S., Mazelle, C., et al. (2016). MAVEN observations of electron-induced whistler mode waves in the Martian magnetosphere. *Journal of Geophysical Research: Space Physics*, *121*, 9717–9731. <https://doi.org/10.1002/2016JA023194>
- Harada, Y., Halekas, J. S., McFadden, J. P., Mitchell, D. L., Mazelle, C., Connerney, J. E. P., et al. (2015). Marsward and tailward ions in the near-Mars magnetotail: MAVEN observations. *Geophysical Research Letters*, *42*, 8925–8932. <https://doi.org/10.1002/2015GL065005>
- Horne, R. B., Wheeler, G. V., & Alleyne, H. S. C. K. (2000). Proton and electron heating by radially propagating fast magnetosonic waves. *Journal of Geophysical Research*, *105*(A12), 27,597–27,610. <https://doi.org/10.1029/2000JA000018>
- Jakosky, B. M., Brain, D., Chaffin, M., Curry, S., Deighan, J., Grebowsky, J., et al. (2018). Loss of the Martian atmosphere to space: Present-day loss rates determined from MAVEN observations and integrated loss through time. *Icarus*, *315*, 146–57. <https://doi.org/10.1016/j.icarus.2018.05.030>
- Jakosky, B. M., Lin, R. P., Grebowsky, J. M., Luhmann, J. G., Mitchell, D. F., Beutelschies, G., et al. (2015). The Mars Atmosphere and Volatile Evolution (MAVEN) mission. *Space Science Reviews*, *195*, 3–48. <https://doi.org/10.1007/s11214-015-0139-x>
- Lillis, R. J., Mitchell, D. L., Lin, R. P., Connerney, J. E. P., & Acuña, M. H. (2004). Mapping crustal magnetic fields at Mars using electron reflectometry. *Geophysical Research Letters*, *31*, L15702. <https://doi.org/10.1029/2004GL020189>
- Lucek, E. A., Constantinescu, D., Goldstein, M. L., Pickett, J., Pinçon, J. L., Sahraoui, F., et al. (2005). The Magnetosheath. *Space Science Reviews*, *118*(1), 95–152. <https://doi.org/10.1007/s11214-005-3825-2>
- Lundin, R. (2011). Ion acceleration and outflow from Mars and Venus: An overview. *Space Science Reviews*, *162*(1–4), 309–334. <https://doi.org/10.1007/s11214-011-9811-y>
- Lundin, R., Barabash, S., Andersson, H., Holmström, M., Grigoriev, A., Yamauchi, M., et al. (2004). Solar wind-induced atmospheric erosion at Mars: First results from ASPERA-3 on Mars Express. *Science*, *305*(5692), 1933–1936. <https://doi.org/10.1126/science.1101860>
- Mazelle, C., Winterhalter, D., Sauer, K., Trotignon, J., Acuña, M., Baumgärtel, K., et al. (2004). Bow shock and upstream phenomena at Mars. *Space Science Reviews*, *111*(1–2), 115–181. <https://doi.org/10.1023/B:SPAC.0000032717.98679.d0>
- McFadden, J. P., Kortmann, O., Curtis, D., Dalton, G., Johnson, G., Abiad, R., et al. (2015). MAVEN SupraThermal and Thermal Ion Composition (STATIC) instrument. *Space Science Reviews*, *195*(1–4), 199–256. <https://doi.org/10.1007/s11214-015-0175-6>
- Meredith, N. P., Horne, R. B., & Anderson, R. R. (2008). Survey of magnetosonic waves and proton ring distributions in the Earth's inner magnetosphere. *Journal of Geophysical Research*, *113*, A06213. <https://doi.org/10.1029/2007JA012975>
- Mitchell, D. L., Mazelle, C., Sauvaud, J.-A., Thocaven, J.-J., Rouzaud, J., Fedorov, A., et al. (2016). The MAVEN Solar Wind Electron Analyzer. *Space Science Reviews*, *200*, 1–34. <https://doi.org/10.1007/s11214-015-0232-1>
- Nagy, A., Winterhalter, D., Sauer, K., Cravens, T., Brecht, S., Mazelle, C., & Trotignon, J. (2004). The plasma environment of Mars. *Space Science Reviews*, *111*(1–2), 33–114. <https://doi.org/10.1023/B:SPAC.0000032718.47512.92>
- Perraut, S., Roux, A., Robert, P., Gendrin, R., Sauvaud, J.-A., Bosqued, J.-M., et al. (1982). A systematic study of ULF waves above FH+ from GEOS 1 and 2 measurements and their relationships with proton ring distributions. *Journal of Geophysical Research*, *87*(A8), 6219–6236. <https://doi.org/10.1029/JA087iA08p06219>
- Posch, J. L., Engebretson, M. J., Olson, C. N., Thaller, S. A., Breneman, A. W., Wygant, J. R., et al. (2015). Low-harmonic magnetosonic waves observed by the Van Allen Probes. *Journal of Geophysical Research: Space Physics*, *120*, 6230–6257. <https://doi.org/10.1002/2015JA021179>
- Ramstad, R., Barabash, S., Futaana, Y., Nilsson, H., & Holmström, M. (2017). Global Mars-solar wind coupling and ion escape. *Journal of Geophysical Research: Space Physics*, *122*, 8051–8062. <https://doi.org/10.1002/2017JA024306>
- Romanelli, N., Bertucci, C., Gómez, D., Mazelle, C., & Delva, M. (2013). Proton cyclotron waves upstream from Mars: Observations from Mars Global Surveyor. *Planetary and Space Science*, *76*, 1–9. <https://doi.org/10.1016/j.pss.2012.10.011>
- Romanelli, N., Mazelle, C., Chaufray, J. Y., Meziane, K., Shan, L., Ruhunusiri, S., et al. (2016). Proton cyclotron waves occurrence rate upstream from Mars observed by MAVEN: Associated variability of the Martian upper atmosphere. *Journal of Geophysical Research: Space Physics*, *121*, 11,113–11,128. <https://doi.org/10.1002/2016JA023270>
- Ruhunusiri, S., Halekas, J. S., Connerney, J. E. P., Espley, J. R., McFadden, J. P., Larson, D. E., et al. (2015). Low frequency waves in the Martian magnetosphere and their response to upstream solar wind driving conditions. *Geophysical Research Letters*, *42*, 8917–8924. <https://doi.org/10.1002/2015GL064968>
- Ruhunusiri, S., Halekas, J. S., Connerney, J. E. P., Espley, J. R., McFadden, J. P., Mazelle, C., et al. (2016). MAVEN observation of an obliquely propagating low-frequency wave upstream of Mars. *Journal of Geophysical Research: Space Physics*, *121*, 2374–2389. <https://doi.org/10.1002/2015JA022306>
- Ruhunusiri, S., Halekas, J. S., McFadden, J. P., Connerney, J. E. P., Espley, J. R., Harada, Y., et al. (2016). MAVEN observations of partially developed Kelvin-Helmholtz vortices at Mars. *Geophysical Research Letters*, *43*, 4763–4773. <https://doi.org/10.1002/2016GL068926>
- Russell, C. T., Holzer, R. E., & Smith, E. J. (1970). OGO 3 observations of ELF noise in the magnetosphere: 2. The nature of the equatorial noise. *Journal of Geophysical Research*, *75*(4), 755–768. <https://doi.org/10.1029/JA075i004p00755>
- Santolik, O., Parrot, M., & Lefeuvre, F. (2003). Singular value decomposition methods for wave propagation analysis. *Radio Science*, *38*(1), 1010. <https://doi.org/10.1029/2000RS002523>
- Taubenschuss, U., & Santolik, O. (2019). Wave polarization analyzed by singular value decomposition of the spectral matrix in the presence of noise. *Surveys in Geophysics*, *40*(1), 39–69. <https://doi.org/10.1007/s10712-018-9496-9>
- Trotignon, J., Mazelle, C., Bertucci, C., & Acuña, M. (2006). Martian shock and magnetic pile-up boundary positions and shapes determined from the Phobos 2 and Mars Global Surveyor data sets. *Planetary and Space Science*, *54*(4), 357–369. <https://doi.org/10.1016/j.pss.2006.01.003>
- Weber, T., Brain, D., Mitchell, D., Xu, S., Connerney, J., & Halekas, J. (2017). Characterization of low-altitude nightside Martian magnetic topology using electron pitch angle distributions. *Journal of Geophysical Research: Space Physics*, *122*, 9777–9789. <https://doi.org/10.1002/2017JA024491>
- Wei, H. Y., & Russell, C. T. (2006). Proton cyclotron waves at Mars: Exosphere structure and evidence for a fast neutral disk. *Geophysical Research Letters*, *33*, L23103. <https://doi.org/10.1029/2006GL026244>

### Erratum

In the originally published version of this article, erroneous values of the proton Alfvén speed were stated. In section 5.2, “48 and 23 km/s” should read “226 and 224 km/s.” We note that the proton ring speed (300-500 km/s, see Figures 2 and 4a) exceeds the corrected proton Alfvén speed. Thus, the conclusions of the paper are unaffected. The text has since been corrected and this version may be considered the authoritative version of record.